

**Aerodynamic Performance Analysis of Axial Fan and
Parametric Optimization of Blade Edges under the
Influence of Boundary Layer Ingestion**



By

Muhammad Awais

Reg. No: 00000360923

Session 2021-2023

Supervised by

Dr. Majid Ali

US-Pakistan Center for Advanced Studies in Energy (USPCAS-E)

National University of Sciences and Technology (NUST)

H-12, Islamabad 44000, Pakistan

December 2023

**Aerodynamic Performance Analysis of Axial Fan and
Parametric Optimization of Blade Edges under the
Influence of Boundary Layer Ingestion**



By

Muhammad Awais

Reg. No: 00000360923

Session 2021-23

Supervised by

Dr. Majid Ali

**A Thesis Submitted to the US-Pakistan Center for Advanced Studies in
Energy in partial fulfillment of the requirements for the degree of
MASTER of SCIENCE in
Thermal Energy Engineering**

US-Pakistan Center for Advanced Studies in Energy (USPCAS-E)

National University of Sciences and Technology (NUST)

H-12, Islamabad 44000, Pakistan

December 2023

Thesis Acceptance Certificate

Certified that final copy of MS/MPhil thesis written by Mr. Muhammad Awais (Registration No. 00000360923), of USPCAS-E has been vetted by the undersigned, found complete in all respects as per NUST Statues/Regulations, is within the similarity indices limit and is accepted as partial fulfillment for the award of MS/MPhil degree. It is further certified that necessary amendments as pointed out by GEC members of the scholar have also been incorporated in the said thesis.

Signature: Majid

Name of Supervisor: Dr. Majid Ali

Date: 01/01/2024

Signature (HOD): Majid

Date: 02 Jan 2024

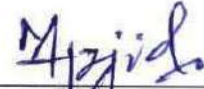
Signature (Dean/Principal): [Signature]

Date: [Signature]

Certificate

This is to certify that work in this thesis has been carried out by **Mr. Muhammad Awais** and completed under my supervision in High-Performance Computing Lab laboratory, US-Pakistan Center for Advanced Studies in Energy (USPCAS-E), National University of Sciences and Technology, H-12, Islamabad, Pakistan.

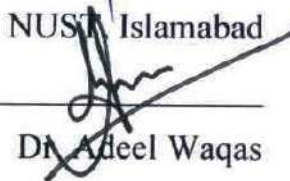
Supervisor:



Dr. Majid Ali
USPCAS-E

NUST, Islamabad

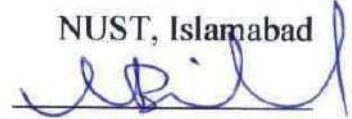
GEC member 1:


Dr. Adeel Waqas

USPCAS-E

NUST, Islamabad

GEC member 2:

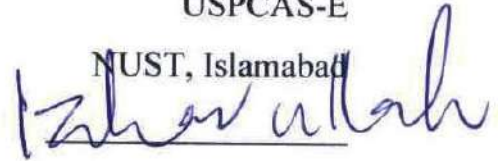


Dr. Muhammad Bilal Sajid

USPCAS-E

NUST, Islamabad

GEC member 3:

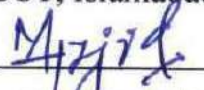


Dr. Izhar Ullah

SMME

NUST, Islamabad

HOD-TEE:



Dr. Majid Ali

USPCAS-E

NUST, Islamabad

Dean/Principal:


Dr. Adeel Waqas

USPCAS-E

NUST, Islamabad

Dedication

Dedicated to my parents who have been my pillars of strength and support throughout my academic journey. I am thankful to my teachers, who have imparted me with valuable knowledge and skills and have inspired me to excel in my field of study. I am indebted to my siblings, who have been my best friends and companions and have cheered me up in times of difficulty. I am appreciative of my friends, who have shared my joys and sorrows and have enriched my life with their friendship. Without their guidance, assistance, and encouragement, this work would not have been possible.

Acknowledgment

With immense gratitude to Allah Almighty, I express my appreciation for the strength and fortitude bestowed upon me, enabling the successful completion of this dissertation. The pursuit of an MS degree has been a challenging yet rewarding journey, replete with valuable life lessons. As I conclude my research, I seize this opportunity to extend my sincerest thanks to my supervisor, **Dr. Majid Ali**, for the unflagging support and guidance rendered throughout the MS program and research.

Furthermore, I express my deep appreciation to my guidance and evaluation committee –**Dr. Adeel Waqas, Dr. Muhammad Bilal Sajid, and Dr. Izhar Ullah** - for their insightful feedback, which significantly enriched the research.

The unwavering support of the teaching and non-teaching faculty of the U.S.-Pakistan Center for Advanced Studies in Energy is also acknowledged for facilitating a seamless research experience.

I extend special recognition to my **Dear Parents**, whose unwavering support served as a beacon of hope and encouragement throughout this journey. **My Friends** and **Colleagues** also deserve commendation for their wholehearted assistance and unwavering encouragement, offering support in every conceivable way.

Muhammad Awaís

Abstract

A non-axisymmetric inlet distortion problem exists in a boundary layer ingesting propulsion system, which seriously affects the aerodynamic performance of the fan. This work presents an in-depth analysis of the fan stage under the influence of boundary layer ingestion. A high-fidelity numerical approach is adopted to quantify the parameters that reduce the isentropic efficiency, total pressure ratio, and stability margin. At a later stage, an artificial neural network-based surrogate mathematical model is used in a multi-objective genetic algorithm to perform optimization. NASA stage 67 has been selected and validated against the experimental data. Entire annulus, steady-state, and three-dimensional modeling have been used for the combined analysis to analyze the effect of the inlet distortion on the fan stage. The numerical results indicated that the isentropic efficiency and total pressure ratio dropped by 9.49 % and 4.1%, respectively. The significant losses occurred at the suction side of the adjacent blade. Based on losses, trailing edge parameters are selected over the span near the blade's tip to ensure robust performance under the fan-face distortion. As a result of optimization, the isentropic efficiency and total pressure ratio improved by 2.88% and 1.69%, respectively. The optimization adds a value near the tip of the blade caused by the improvement of shockwave.

Keywords:

Non-axisymmetric Distortion; Boundary Layer Ingestion; Transonic Fan Blade; MOGA; Aerodynamic Design Optimization

Table of Contents

Abstract.....	VI
List of Figures.....	X
List of Tables	XII
List of Publications	XIII
List of Abbreviations	XIV
Chapter 1 Introduction.....	1
1.1 Background.....	1
1.2 Research Gap	2
1.3 Aims and Objectives.....	3
1.4 Present Work	4
Summary.....	5
Chapter 2 Literature Review	6
2.1 Types of Thrust Distribution Method	6
2.1.1 Distributed Exhaust.....	6
2.1.2 Cross Flow Fans.....	7
2.1.3 Multiple Discrete.....	8
2.2 Power Transmission of Thrust Distribution Systems	9
2.2.1 Internal Combustion Engine	10
2.2.2 Electrochemical Cells	10
2.2.3 Hybrid Electric Power Systems	10
2.3 Classification of Aircraft Configuration	10
2.3.1 Aft-Tail.....	10
2.3.2 Tandem Wing.....	11
2.3.3 Tailless	11
2.4 Classification of Distortion.....	12
2.4.1 Total Pressure Distortion	12
2.4.2 Total Temperature Distortion.....	13
2.4.3 Swirl Distortion.....	13
2.5 Rotor Interaction	16
2.6 Optimization	16
Summary.....	18
Chapter 3 Review of Numerical Models and Optimization Techniques	19

3.1	Review on classification of Numerical and Analytic Model.....	19
3.1.1	Actuator Disk Model.....	19
3.1.2	Vortex Method.....	19
3.1.3	RANS.....	20
3.2	Classification Design of Experiment.....	20
3.2.1	Full Factorial and Fractional Factorial Experiment.....	20
3.2.2	Fractional Factorial Experiment.....	21
3.2.3	Surface Response Method.....	21
	Summary.....	22
	Chapter 4 Implementation of CFD for Axial Fan for Inlet Distortions.....	23
4.1	Outline of the Study.....	23
4.2	Case Study.....	23
4.2.1	Computational Domain and Blade Parameter.....	23
4.2.3	Grid Processing and Sensitivity Analysis.....	24
4.2.3	Solver Setup.....	25
4.3	Optimization Methodology.....	26
4.3.1	Box Behnken Design (BBD).....	27
4.3.2	Surrogate Model.....	28
4.3.3	Multi-Objective Optimization.....	28
	Summary.....	29
	Chapter 5 Results and Discussion.....	30
5.1	Validation.....	30
5.2	Baseline Case Stage Flow Field.....	31
5.2.1	Fan Face Flow Field.....	31
5.2.2	Rotor Flow Field.....	34
5.2.3	Stator Flow Field.....	36
5.3	DOE-Based Baseline Optimized Test.....	37
5.4	Optimized Case Rotor Flow Field.....	38
5.4.1	Fan Face Flow Field.....	38
5.4.2	Optimized Rotor Flow Field.....	39
5.4.3	Optimized Case Stator Flow Field at Downstream Face.....	42
5.4.4	Optimized Flow Field at Duct-Outlet.....	43
5.4.5	Blade to Blade Comparison:.....	45

Summary.....	47
Chapter 6 Conclusions and Recommendations.....	48
6.1 Conclusions.....	48
6.2 Future Prospects.....	48
References.....	50
APPENDIX-I.....	54

List of Figures

Figure 1.1	Fan faces boundary layer in blended wing body aircraft.....	2
Figure 2.1	Distributed Exhaust Propulsion system.....	6
Figure 2.2	Internal duct at trailing edge of wing span	7
Figure 2.3	Cross flow Propulsion system	7
Figure 2.4	Cross flow fan application in aircraft	8
Figure 2.5	Distributed discrete fan in blended wing body and podded engines	9
Figure 2.6	Load distribution in podded engines	11
Figure 2.7	Aerodynamic Lift distribution in blended wing body	12
Figure 2.8	Boundary layer distribution in different configuration of aircraft.....	13
Figure 2.9	Type of swirl a) Bulk swirl b) Pair swirl c)Tightly wound vortex d) Cross flow wind.....	14
Figure 2.10	Representation of co-swirl and counter swirl.	14
Figure 2.11	Paired swirl in s-duct.	15
Figure 2.12	Tightly vortex generated in Podded engine.....	15
Figure 4.1	Representation of computational domain s-duct and NASA rotor 67.....	23
Figure 4.2	Representation grid around rotor and stator blade normalized span	25
Figure 4.3	Methodology adopted for optimization.	27
Figure 5.1	Validation of transonic fan NASA rotor 67 and stage 67B	30
Figure 5.2	Normalized axial velocity at fan upstream and fan face.	31
Figure 5.3	Non-uniformities at fan face in static pressure, stagnation pressure,swirl angle, radial velocity	32
Figure 5.4	Fan face distortion in incidence angle, normalized axial velocity and swirl angle at 30%span, 60%span, and 90%span.	33
Figure 5.5	Swirl angle and normalized axial velocity at rotor exit.....	34
Figure 5.6	Rotor downstream face contour.....	35
Figure 5.7	Swirl angle at stator face and incidence angle.....	36
Figure 5.8	Isentropic efficiency and Total temperature ratio at stator downstream	37
Figure 5.9	Pareto front of optimized blade	38
Figure 5.10	Comparison of baseline and optimized flow field.....	39
Figure 5.11	Optimized and baseline contour comparison.....	40
Figure 5.12	Optimize total pressure ratio, normalize axial velocity and swirl angle compare with baseline at 30%span, 60%span and 90%span	41

Figure 5.13 Optimized and baseline contour comparison at stator downstream42

Figure 5.14 Isentropic efficiency total pressure ratio and normalized axial velocity contour comparison at duct downstream.44

Figure 5.15 Blade to comparison of contour between optimized case and baseline with respect to Mach number and total temperature ratio at 90% span46

List of Tables

Table 4.1	Blade parameter of NASA stage 67B	24
Table 4.2	Trailing edge parametrization bounds of the rotor blade	27
Table 5.1	Comparison of objective functions	38

List of Publications

1. **Muhammad Awais**, Majid Ali, Talha Bin Tahir, Qazi Shahzad Ali, Izhar Ullah, Deepak Kumar “Aerodynamic Performance and Parametric Optimization of Blade Edges Under the Influence of Boundary Layer Ingestion”
Journal: Propulsion and Power Research, 2023 (**Under Review**)

List of Abbreviations

Abbreviations

BLI	Boundary Layer Ingestion
BWB	Blended Wing Body
DOE	Design of Experiment
MOGA	Multi Objective Genetic Algorithm
RPM	Revolution Per Minute
SPL	Sound Pressure Level
TTR	Total Temperature Ratio
TPR	Total Pressure Ratio

Symbols

C	Velocity
CO ₂	Carbon Dioxide
D	Drag
J	Joule
M	Mach Number
S	Static Entropy
T	Trailing edge
U	Blade Velocity
α	Swirl angle
η	Isentropic Efficiency
π	Total Pressure Ratio

Subscript

A	Axial
R	Radial
1	Rotor Outlet
2	Stator Outlet
3	Duct Outlet
o	Stagnation Quantity

Chapter 1 Introduction

1.1 Background

Civil aviation plays a vital role in transportation; it is one of the most devastatingly growing sectors in transportation. The rapid growth in air transportation causes significant consequences for the environment. The environmental impacts caused by air transportation are fundamentally divided into aircraft noise and the emissions as a result of the combustion of fuel. These pollutants affect the air quality in the environment and atmospheric life. Hence, the direct emission of CO₂ into the atmosphere plays a vital role in climate change. Globally, 918 million metric tons of CO₂ were produced in 2018, including 2.4 % of worldwide CO₂ from fossil fuel use. These emissions considerably increased by about 32% over the last five years [2]. Special attention is required to protect the environment. Several legislative initiatives have been conducted to achieve these significant milestones: 1) a cap on net aviation CO₂ from 2020 (carbon-neutral growth); 2) a reduction in net aviation CO₂ emission of 50 % by 2050, relative to 2005 levels; 3) An average improvement in fuel efficiency of 1.5 % per year from 2009 to 2020[3]. Although the International Air Transport Association (IATA) introduced a strategy to achieve these milestones, all the stakeholders agreed on this ‘four pillar strategy’ composed of improved technology, more efficient aircraft operation, infrastructure, and economic measures [3].

Several innovative technologies are currently being attempted with different structural configurations to reduce emissions. Non-conventional aircraft blended wing body (BWB) is one such technology in which boundary layers were ingested (BLI) into the propulsion system. However, it theoretically reduces fuel combustion by up to 15% compared to conventional planes [4]–[6]. In the BWB aircraft, engines are integrated into the cylindrical fuselage at aft the airplane with a broader span. Therefore, it reduces the wetted area to a volume ratio and decreases the skin friction, which helps increase the lift-to-drag ratio (L/D) up to 20%. The fan face ingests the boundary flow of the airframe, which is re-energized by the fan stage, reduces the wasted kinetic energy, and increases the propulsive efficiency of the aircraft [7].

As the flow enters the fan face, non-uniform pressure distribution in BLI flow leads to the attenuation of axial velocity toward the casing at the upstream of the fan. The highly distorted flow captured at intake of fan face reduces the fan performance caused

by radial flow distribution. The inlet distortion flow field generates circumferential and radial variation in the diffusion factor with loss variation around the annulus.

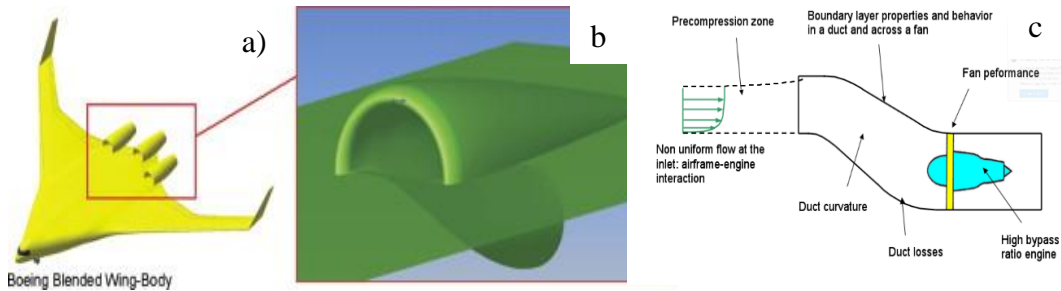


Figure 1.1 Fan faces boundary layer in blended wing body aircraft.

1.2 Research Gap

As the boundary layer grows in duct a non-uniform flow observes at fan face. The flow is no longer to be an axis symmetric that required a special attention to perform a high-fidelity simulation. Most of the up-to-date research is done up on stage analysis S67A. The pressure ratio distribution was varying uniformly from 0.9 to 1 at fan face. In this type of analysis, the inlet pressure non-uniformity is much lower, and the Nose signature is too high. But the major research gap still left In new configuration of aircraft where engines were embedded over the aft of surface. While In BWB configuration fan were embedded into the frame of aircraft that significantly affect the performance of fan.

As most of researchers performed a CFD analysis on simple s duct and redesign it to improve the flow characteristics. To capture a boundary layer a lot of research has been done on the whole analysis of body to take insight idea about the flow separation in blade channel without s duct. Therefore, very little research on redesigning a blade in order to optimize the performance of efficiency and pressure ratio. As the flow moves toward the fan face the non-uniformity in static pressure is too high that reduce the efficiency, pressure ratio and stability margin is evidently suffer this research focus to predict the losses stability margin along with significantly decrease in efficiency and Pressure ratio.

Most of the research has been done on transonic fans to optimize the efficiency and pressure ratio by injection of mass flow at the wake region of blade therefore a gap in research still left in redesigning of blade under high inlet distortion. The whole stage continuously working under high fatigue, required attention to simulate the fluid structure interaction (FSI) analysis to observe wear and tear analysis. A major gap in research is up to date remained behind to operate a fan with different Speed line to optimize its performance. As the flow pass out through the stator blade its efficiency significantly drop due to high swirl generated by the rotor hence another gap in research to change the angle of attack of stator to overcome this factor in a specific region where the intensity of co swirl is high or to optimize the blade

The noise level is significantly decreased in BLI that need the transient acoustic analysis at different height with different cruise condition. Therefore, the inlet distortion still increases the sound level due to velocity fluctuations in the vicinity of fan.

One of the most significant parameters is to reduce the inlet distortion by using the boost trap fan at the rotor face or by installing the addition inlet guide van. The guide van helps to reduce the flow distortion by changing the direction of flow in a s duct. While boost trap fan helps to reenergize the flow in the wake region of s duct. Addition factor to remove the boundary layer by adding the extra outlet in duct or to re-energies to slowly moving boundary layer by adding clean flow to increase the efficiency pr and stability margin.

1.3 Aims and Objectives.

The focus of this study to optimize the leading edge for designing distortion-tolerant fan stage. This study targets to explore the fan performance and detailed flow topography when subjected to boundary layer ingestion and design distortion tolerant fan stage for improved performance under the influence of BLI.

These are the following objectives of this study that were widely adopted in this research.

- To model the rotor and stator by using the Ansys Module blade gen.
- To validate the rotor model with the experimental compressor map performed at the Lewis research laboratory.
- To validate the whole stage 67B with experiment to justify the stator model.
- To model the serpentine diffuser and check its Pressure recovery.

- To study the effect of non-axisymmetric flow field on the performance of axial fan stage.
- To optimize the blade tip clearance and leading edge of blade at different span locations for an improved flow field.
- To perform a sensitivity analysis of the objective functions for different input parameters.

1.4 Present Work

This work presents the optimization of whole stage to reduce the flow separation in a stage channel by optimizing the incidence angle from negative to positive and reduce the swirl angle that directly affects the performance of whole stage. The whole work present in detail in the following chapter

Chapter 2 presents the thrust distribution that involves various configurations along with the power source of thrust and classification of aircraft configurations. These thrust distributions were widely applicable in aircraft configuration. Therefore, the thrust distribution and configuration of aircraft changes different types of flow distortion occur that widely affect the performance of system.

Chapter 3 would explain the different types of analytic model that were extensively used to reduce the computation cost. To analyze the flow behavior in certain conditions without an actual model. It also gives insight idea into the flow behavior as result of changing the whole model. The different types of design of experiment are also described that are used to conclude the behavior by changing the boundaries in certain limit of same parameters. That were used to predict the accuracy of fitness function.

Chapter 4 describes the methodology that was adopted for the modeling of fan, stator, and duct. The grid sensitive analysis is performed to select the appropriate mesh. The solver setup is validated against the experiment with the same boundary condition. A single passage is run to validate the model. Therefore, the s duct is coupled to conclude the effect of boundary layer on the performance of stage. The optimization tool Multi objective genetic algorithm is used to optimize the objective functions pressure ratio and efficiency of whole model.

Chapter 5 concludes the graphical representation of validation of model. The effect of BLI on the performance of whole stage, how the incidence angle affects the total pressure ratio and total temperature ratio. The flow separation is also discussed in baseline case. Furthermore, the optimized case is compared with the baseline case.

Summary

This chapter gives a very brief idea about non-uniformities occur in a static pressure in Blended wing body aircraft due to boundary layer ingestion. As the moves toward the fan face the flow transport from upper portion to lower portion. The main research gap in this project is FSI analysis, two-way FSI. The effect of BLI on the performance of stage 67 A. the effect of angle of attack of stator on the performance of stage under BLI. In this research the focus is to conclude the effect of fan performance under high inlet distortion.

Chapter 2 Literature Review

2.1 Types of Thrust Distribution Method

The thrust distribution is a fundamental characteristic of every aircraft configuration. Therefore, with the advancement of technology to reduce the emission of fuel different types of thrust, power source and configuration of aircraft were designed. The use of mono lithic engines was extensively used till widespread wingspan configuration which are commonly used for commercial transportation. In future advanced distribution thrust propulsion systems are designed to make transportation clean and more effective. These are the following types of thrust distribution method.

2.1.1 Distributed Exhaust

The first configuration is jet flaps in which the exhaust of aircraft is ducted through the narrow section of trailing edge or through the slot near it. That provides a high thrust during the landing, take off and used for high supercritical lift. Some of them are called distributed exhaust. In this configuration the direction of exhaust is changed and further utilized to increase the thrust. Therefore, engine exhaust distributed through multiple slots at the trailing edge as result its propulsive efficiency increases.

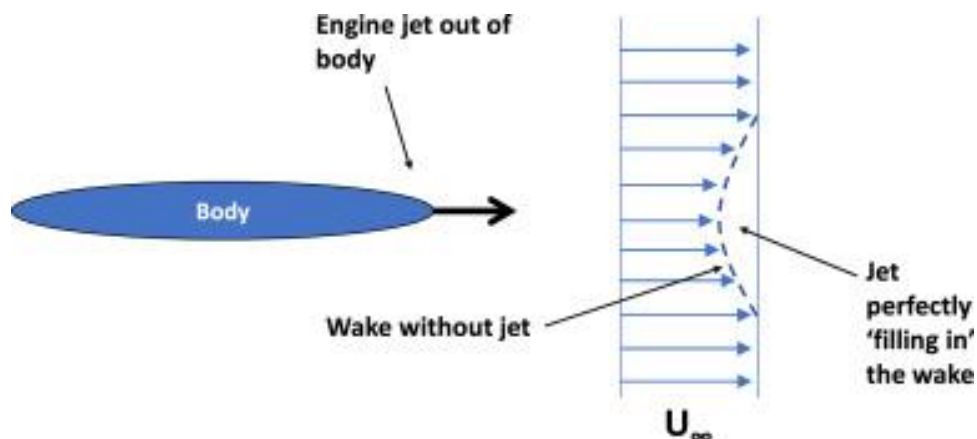


Figure 2.1 Distributed Exhaust Propulsion system

This figure represents the flow behavior when the pass through the wing at the trailing edge of wing it is clearly show the wake region behind them. The deficit of flow in this region cause to decrease the efficiency of System hence the exhaust flow pass through internal duct at trailing edge that increase the thrust as represent below.

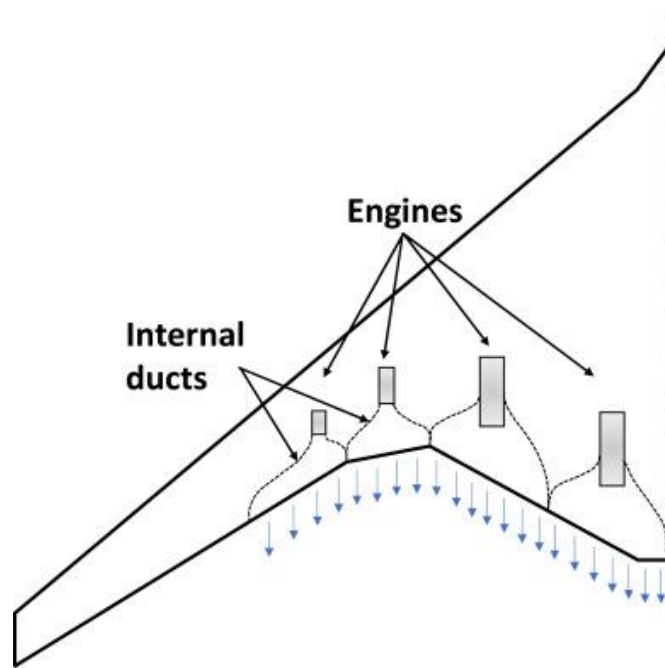


Figure 2.2 Internal duct at trailing edge of wing span

Whereas duct exhaust not only promising this wake to cover the jet flap is another possible use of this technology, where a slit at or near the wing's trailing edge emits a high-velocity thin jet sheet that provides span wise thrust for cruise.

2.1.2 Cross Flow Fans

Cross flow fan distribution is a totally different form of thrust distribution system. In which fan is not rotating around the parallel axis to the motion of plane. Therefore, in this configuration the fan is rotating perpendicular to the motion of plane.

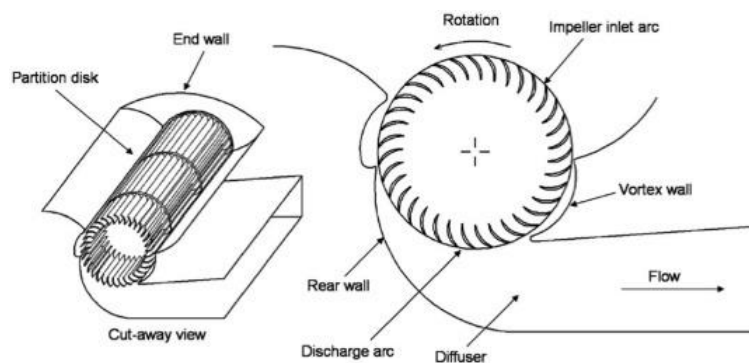


Figure 2.3 Cross flow Propulsion system

The fan is enclosed in drum whereas the blade of fan is forward curved around the drum, and it extended across wingspan. They have rectangular inlet and outlet. The main advantage of this configuration is that they are produced uniform in flow and out flow. This fan design is proposed by Dornier and are widely used in HVAC systems. This type of fan is driven by internal combustion engine, gas turbine and through electric motors. They have a single fan on wingspan but multiply fan over the span that are coupled between them. This fan has wake filling properties like jet faps the fan outlet flow is located at trailing edge of wingspan, that increase the propulsive efficiency due to active boundary layer.



Figure 2.4 Cross flow fan application in aircraft

This fan is examined by fan wing LTD with cooperation of German aerospace (DLR). This fan has short takeoff and landing aircraft as helicopters. The lower speed of this thrust distribution led to safely use for agriculture on large scale.

2.1.3 Multiple Discrete

In multiple discrete thrust distribution systems axial fan flow is used that is widely applied to huge number of different types of aircraft, which commonly used for transportation of goods and passengers.

In this category two or more large size fans are used like AN-225 on the span wise direction. In this category the axial fan rotates along the axis of motion of plain. The number of RPM depends upon the size of the fan. The larger the fan, the lower will be the fan speed the world largest weight carrying aircraft. They have six axial flow fans at wingspan. So, the same type of axial fan flow is also used in different types of aircraft configuration in which the smaller size of axial fan is installed over the airframe. There is no any upper limit of individual number of axial fan or propulsor used over the airframe. In this type of propulsion system fan ingest the boundary layer to reduce the noise level and decrease the combustion of fuel so these types of propulsion used in blended wing body aircraft that reduce the weight of whole-body aircraft. In this project used the s duct to analyze the behavior of boundary layer on performance of axial flow fan this is NASA short takeoff and landing aircraft with 12 turbofans install over the airframe of aircraft.



Figure 2.5 Distributed discrete fan in blended wing body and podded engines

2.2 Power Transmission of Thrust Distribution Systems

Globally to reduce the emission of fuel several propulsion systems were examined to build aviation industry green. Aircraft propulsion systems are characterized by thrust distribution and power transmission. In general power is transmitted through the gear but different types of sources are utilized to drive the fan. Some of them are very commonly applied in this decade, some of them very unconventional. The pneumatic

power source is one of them in which fan is drive through the nozzle but did not widely apply at commercial level due to design limitations.

2.2.1 Internal Combustion Engine

The conventional aircraft is highly dependent upon the internal combustion engine. Therefore, the piston and gas turbine engine are used in DP system that are widely available in literature. The focus is to replace the fuel whose cost is low and combustion efficiency is high. The hydrogen-based fuel is applied in N3-X concept require a low temperature storage as a result it also used for cooling of superconducting as a fuel itself although its cost is very high. Another cryogenic fuel methane has a high consideration to use as fuel in aviation industry, it has lower cost as per energy than other fuel.

2.2.2 Electrochemical Cells

The drive of DP configuration in aerial vehicle is highly dependent on batteries. In which batteries are installed that convert chemical energy to electrical, furthermore the electrical energy converts into mechanical energy by using the motor. In future this technology will be tremendously applied for green transportation although a lot of research work is in progress due to its high cost. Therefore, multiple Distributed propellers will also work on this technology in future according to aviation industry.

2.2.3 Hybrid Electric Power Systems

This concept is based upon the central generator that is installed at the aft of fuselage that transmits electrical energy to the propellers. This technology covers the gap between the energy density in electrochemical and liquid chemical fuel in internal combustion. This arrangement is used in the NASA N3-X TEDP proposal, and it has also been suggested by Airbus/EADS in their E-thrust concept.

2.3 Classification of Aircraft Configuration

DP designs need a high degree of integration between the structure, aerodynamics, and propulsion systems of an aircraft design. To adopt a new technology of DP it requires a new architecture design that are compatible with DP. These are the following configuration of aircraft design.

2.3.1 Aft-Tail

This is a conventional aircraft that is referred to be a tube and wing. The load distribution is non-uniform in this case. The skin friction coefficient is high as compared to other cases that reduce the L/D ratio and as a result its efficiency drops.

The inertial load is very high as compared to other. Therefore, HPES is practically used in this configuration of airplane that reduces the 3% reduction in fuel consumption.

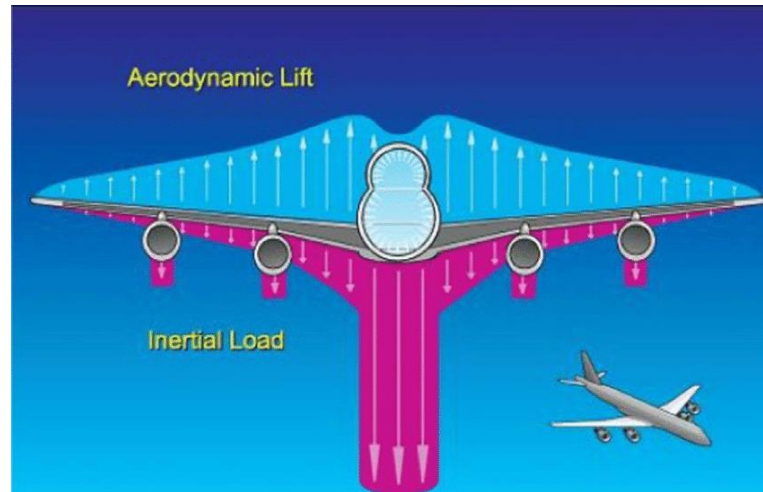


Figure 2.6 Load distribution in podded engine

2.3.2 Tandem Wing

In this configuration airplane have two wing one at forward and the second is at the rear. The chord length of the second wing is equal to the first wing. The lift forces on the two wings of a tandem wing are longitudinally separated, enabling them to work together to generate stability, control, and trim. The stability and control mechanisms of a tandem wing are comparable to those of a tail-first or canard configuration; the key difference is the relative size of the front surface.

2.3.3 Tailless

Blended wing body is a type of tailless aircraft configuration. BWB aircraft engines are integrated into the cylindrical fuselage of airplane with wider span. which reduces the wetted area to a volume ratio and decreases the skin friction that helps to increase the L/D ratio up to 20%.

The multiple DP configuration is used in this case that over all reduce its weight. The prototype of this model is tested but still in re-designing phase. When the boundary layer ingested by the fan it noses signature is reduce but the stability margin and efficiency is drop due to the inlet distortions at fan face.

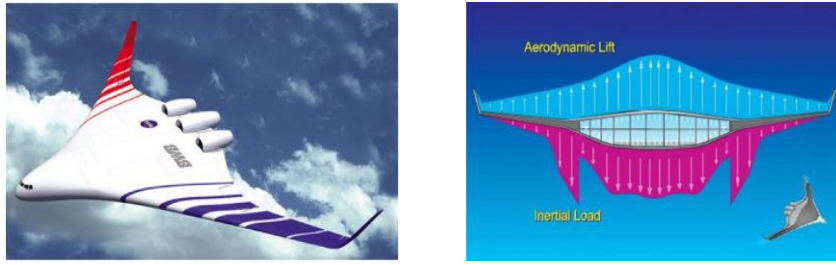


Figure 2.7 Aerodynamic Lift distribution in blended wing body

2.4 Classification of Distortion

While the different configurations give complex distortion at the fan face, they may be loosely categorized based on their impact, pattern, motion state, or duration time. Therefore, the distortion is categorized by inlet pressure distribution, total temperature distribution and swirl distribution are locally categorized by its location radially and circumferentially. Furthermore, this distortion is dependent upon either the stationary distortion or rotating distortion which relate to duration time. These are the following types of distortions.

2.4.1 Total Pressure Distortion

As the flow passes through the nacelle of aircraft it possesses a pressure distortion at fan face due to the boundary layer ingestion. Another reason for pressure distortion is also faces due to the crosswind flow at fan face. this pressure distortion may occur circumferentially and radially.

This pressure distortion reduces the stability margin of axial flow fan and the efficiency of fan also reduced due to off design in flow condition. Pressure distortion is also examined circumferentially and radially Reid et al conclude that circumferential distortion badly effects the stall margin. While this effect is overcome by the delivery pressure into several portions of equal area.

This figure represents the total pressure distortion in different configurations of aircraft. The first figure represents the pressure distortion at the aft of tube. When the flow passes the tube of aircraft that generates a boundary layer effect circumferentially around the hub. The second picture shows the boundary layer growth in double bubble D8 aircraft in which fan captures the boundary layer that increases the flow separation around the blade. Therefore, in figure they ingest the boundary from the side of tube where the fan embedded at side of tube.

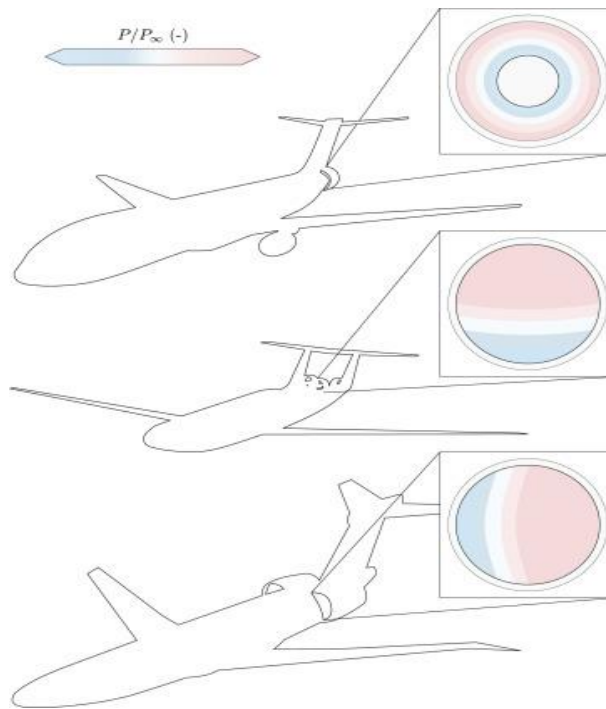


Figure 2.8 Boundary layer distribution in different configuration of aircraft

2.4.2 Total Temperature Distortion

The total temperature distortion is very low in a true manner but occurs in a certain condition. This type of distortion is mostly useful for military purposes by ingesting steam for catapult, launching pads by ingestion hot gases and use for reverse thrust during the landing. The TPD commonly reduces the efficiency and stall margin of compressor therefore it also occurs slight due to pressure distortion at fan face. The stability of the downstream components, such the combustion chamber, will be impacted by the propagation of the total temperature distortion from the upstream components.

2.4.3 Swirl Distortion

As the flow propagates towards the fan, swirls are generated due to crosswind, boundary layer ingestion, rotation of flow around the spinner and non-uniform static pressure at the fan face. Due to non-uniform inlet static pressure at the fan face, flow migrates from region high pressure to lower pressure in a radially direction that generates the swirl. Swirl is the key parameter that represents the distortion in flow. It is the angular deviation between local velocity vector and normal velocity vector in a cylindrical plane. Further swirl distortion was categorized into four types.

- Bulk Swirl
- Pair swirl
- Tightly Wound Vortex
- Cross flow swirl

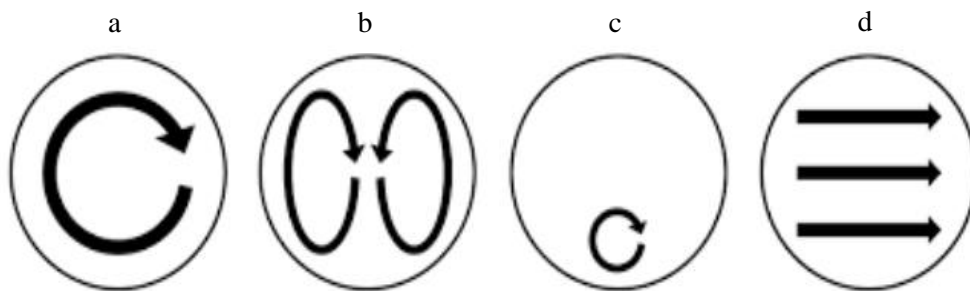


Figure 2.9 Type of swirl a) Bulk swirl b) Pair swirl c) Tightly wound vortex d) Cross flow wind

The bulk swirl is generated when whole flow field is rotate about the axis of the engine. This type of swirl is called co swirl while if the swirl direction is opposites to the rotation of axis is called the counter swirl.

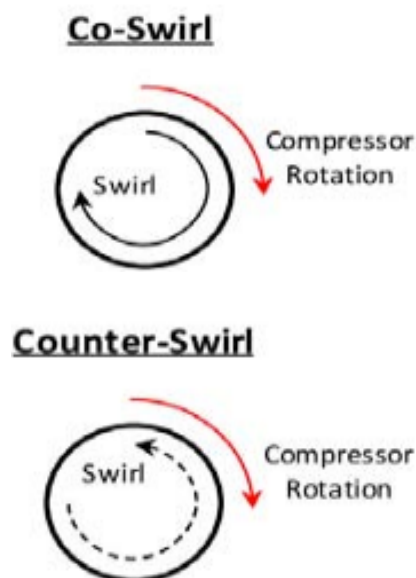


Figure 2.10 Representation of co-swirl and counter swirl.

As the flow is non-axis-symmetric experiences a total pressure gradient normal to plane in s duct. The representation of co swirl and counter swirl is shown in figures.

The Paired swirl is developed when the flow passes through the duct. The lower momentum flow combined with high momentum flow due to velocity difference at plane within a duct. The second reason is the vorticity vector which is turned by curvature of a s-duct. As the velocity is zero due to boundary layer near the wall and it will be maximum at the core of duct, momentum is distributed accordingly. The type of swirl generally consists of two more vortices rotating in opposite directions. If the magnitude of the two vortices is equal, then it will be twin paired swirl.



Figure 2.11 Paired swirl in S-duct

A tightly wound vortex is generated at the ground level or near the surface of the airplane. A ground vortex swirl is highly energetic and generated by mechanisms such as tip vortices, an extension of the leading edge, and static operation near ground proximity.



Figure 2.12 Tightly vortex generated in Podded engine.

The crossflow swirl is generated in straight inlet duct. Meanwhile it is closely related to parried swirl. Therefore, the velocity flow is uniform in pair swirl but in cross flow field velocity is not uniform and flow is normal to fan face.

2.5 Rotor Interaction

The non-uniform flow reduces the aerodynamic stability, performance, and stall margins of fan. The radial distribution flow generates the co-rotating and counter rotating vortices. The co-rotating vortices are ingested into the hub cause the drop in pressure ratio, corrected mass and fan loading [9]. While the counter vortices don't affect the efficiency of compressor. Sieradzki et al. [10] Studied the effect of the BLI on the stall margin of fan. The result shows that 48% reduction in stall margin experimentally due to the inlet distortion. The compressor stalls when the clean flow region fail to remove the separated flow in a passage of a higher incidence angle. Therefore, injectors are installed at the tip section to enhance the stall margin and mitigate flow separation by restricting the higher incidence angle. Zhang et al. [11] performed an experimentation to energize the mass flow at tip section by installing the injectors. The mass flow rates are 0.66% and 1.2% at three positions of constant 85% Speedline of fan. The result indicated that by the injection of mass at a higher angle (350°) degrees yielded the best performance. This injection angle increased the total pressure ratio (PR), improved the stall margin and maintained the fan efficiency. The isentropic efficiency, TPR, TTR and stability margins are highly dependent upon the Speed line. Results demonstrate that increase in Speed line cause to increase the pressure ratio, decrease the stall margin and increased the efficiency to a certain limit after that it drop significantly [12].

2.6 Optimization

Shahsavari at el. [13] Develop a computer program to extract the span wise distribution parameters of 3-dimensional blade. To optimize the axial flow fan by constant the de-Haller number and radial equilibrium equation to increase the performance. The optimized blade has a lower area, sharper leading, trailing edge and larger chamber angle due to high loading. As a result, high pressure ratio due to chord distribution is shorter at hub and larger at tip. However, it makes the hub section narrow, caused to increase the stress at the root of blade. Another method to increase the performance of blade by adding the tandem blade at the suction and pressure side of the rotating blade. Ma at el [14]performed the optimization of two stage rotor 67 as the stall margin and adiabatic efficiency are the objective function of this study. He concludes that 17.2% increased in a stall margin and 2.96% increase in efficiency as result of optimization of blade. Kim at el. [15] used the Latin hypercube model to construct the Surrogate

model to simultaneously increase the efficiency and decrease the Sound level. The genetic algorithm is used to optimize the single objective function while multi-objective function is used to optimize more than one objective function. Results indicate that Genetic algorithm improved total efficiency by 1.90%, while through MOGA 2.20% improvement in efficiency and 0.44 dBA in SPL. Samadat el. [16] optimized the rotor 37 and conclude that 1.4% relatively increase in rotor efficiency along with pressure ratio and temperature ratio. Wang at el.[17] used the hybrid optimization algorithm to optimize the rotor 37 result conclude that 1.8% increase in pressure ratio and 0.8% increase in efficiency.

Summary

In this chapter different types of thrust distribution method were discussed that are commonly used for different application therefore the distributed multiple discrete fans will used in future to improve the propulsion of aircraft along with hybrid electric power systems. The tailless wing configuration used in this thrust distribution system faces a total pressure distortion which leads to a decrease in the performance of the system. As the boundary layer ingests into the duct of blended wing body that reduces the efficiency, pressure and stability margin of fan. The optimized blade has sharper leading edge that leads to an increase in the aerodynamic performance of blade. Different researchers adopt different methodologies to increase the efficiency of fan by varying different parameters.

Chapter 3 Review of Numerical Models and Optimization Techniques

3.1 Review on classification of Numerical and Analytic Model

Several numerical methods and approaches have been developed to estimate the fan performance with the experimental data under inlet distortion. All these methods give adequate information about the performance of the fan through CFD under different operating conditions. Moreover, it is far less expensive and saves time as compared to testing, where the costs for conducting experiments are too high. Due to the rapid growth of CFD analysis for investigating diverse bodies at high Mach numbers, its widespread use is preferred. These studies need high Mach number wind tunnels, which are more expensive to build the experimental setup for the analysis. Hence the new design required crashed analysis or FSI analysis to find the frequency mode and damage of body. These analyses cause great destruction in the experimental setup, so CFD analysis is preferred with different numerical model finite volume method and finite element method. The finite volume method applied for flow analysis of complex bodies based on Navier Stroke equation while. The finite element method is used for the structural analysis of a body both were used during the fluid structure analysis to predict the effect of flow on the structure.

3.1.1 Actuator Disk Model

Wind farms are growing as the market for wind energy expands that requires special attention to analyze the behavior of air around the farm[18]. Analyzing the flow behavior using CFD in windfarm gives better understanding about the vortices generated between the wind turbine that required a huge computational cost to mesh the whole farm with actual wind turbine. Thus, an actuator disk model is a simplified model that is used in CFD analysis to estimate the aerodynamic performance of a wind turbine in a whole wind farm[19]. which further categorized by actuator line model and actuator surface model both have different application according to application.

3.1.2 Vortex Method

The vortex method is a numerical methodology for simulating fluid flow characteristics. It is frequently used in computational fluid dynamics (CFD) to investigate complex flows seen in aerodynamics, weather prediction, and fluid

transport. The approach is especially useful for examining flows with vortices which further classified to vortex line and vortex blobs method[20] [21].In 1931, following the time movement of a system of point vortices to approximate the motion of a two-dimensional vortex sheet. For simulation purposes, the vorticity that was initially focused along a line in two dimensions (vortex sheet) was concentrated even more into a finite number of point vortices. Numerous researchers have employed vortices with limited cores or vortex blobs in these simulations. As a result, using distributed vortex cores or vortex blobs produces more realistic vorticity distributions and bounded induced velocities for all vortex elements.

3.1.3 RANS

Reynolds-averaged Navier-Stokes equations (RANS) models are the most cost-effective method for computing complex turbulent industrial flows. The k- or k-models in their various variants are typical examples of such models [22]. These models reduce the problem to two extra transport equations and introduce an eddy-viscosity (turbulent viscosity) to compute the Reynolds stresses [23]. More advanced RANS models are available that directly solve an equation for each of the six independent Reynolds stresses (RSM) plus a scale equation (-equation or -equation). RANS models are appropriate for many engineering applications and often provide the requisite level of accuracy.

3.2 Classification Design of Experiment

In the Design of an Experiment that is planned, the data-generating process is actively changed to enhance the information's quality and get rid of extraneous data. Obtaining data as sparingly as feasible while providing sufficient details to precisely estimate model parameters is a common goal of all experimental designs. There are several types of design of experiments is available to predict the behavior of results by varying the design properties as following.

3.2.1 Full Factorial and Fractional Factorial Experiment

It is widely acknowledged that full factorial designs at 2- and 3-levels are the most frequently utilized experimental designs in manufacturing firms. An investigator could examine the combined impact of the factors (or process/design parameters) on a response using factorial designs. Factorial designs come in whole and factorial varieties.

A complete factorial planned experiment includes all conceivable level combinations for all components. The total number of experiments required to investigate k factors at two levels is 2^k [24]. The 2^k complete factorial design is extremely effective in the early phases of experimental work, especially when there are fewer than or equal to four process parameters or design parameters (or factors).

3.2.2 Fractional Factorial Experiment

Often, experimenters do not have the time, resources, or budget to conduct FFEs. Suppose the experimenters can reasonably infer that certain higher-order interactions (third order and above) are unimportant. In that case, only a subset of the FFE can be run to collect information on the main effects and two-order interactions. A fractional factorial design is a sort of orthogonal array design that allows experimenters to explore primary effects and desired interaction effects in a limited number of trials or experimental runs.

In industry, fractional factorial designs are the most popular and commonly utilized type of design. These designs are typically written as $2^{(k-p)}$ [25] where k is the number of factors, and $1/2^p$ is a portion of the full factorial 2^k . For example, $2^{(5-2)}$ is a $1/4$ th fraction of a 25 FFE. This means that instead of 32 trials, eight experimental trials might be used to analyze five components at 2 levels.

3.2.3 Surface Response Method

Box and Wilson¹ introduced a response surface methodology (RSM) as a collection of mathematical and statistical tools used to analyze data using an empirical model. Which is further categorized by box behnken and central composite design. A BBD gives a higher-order surface response with fewer runs[26]. It is a class of rotatable second-order design. The number of DOEs is generated based on $N=2k(k-1)+C_0$. (Where k is the number of factors and C_0 is the number of central points on the face)[27]. The points at the center of the experimental domain and the “star” points outside this domain make it possible to estimate the curvature of the response surface. Therefore, these are the main classifications that were used in CFD. Furthermore, the DOE method available in open literature includes d-optimal design, Latin hypercube and quasi-random design.

Summary

This chapter discusses the actual and analytic methods that are widely used in CFD. An actuator disk model is an analytic model while the flow behavior or solution is extracted on the basis RANS equation. Furthermore, it discusses the design of the experiment technique used to predict the behavior concerning the time and computational cost.

Chapter 4 Implementation of CFD for Axial Fan for Inlet Distortions

4.1 Outline of the Study

A well-accredited, high-performance, low aspect ratio transonic fan, NASA Rotor 67, has been selected for the study boundary layer ingestion (BLI). CFD rotor model validated against the experimental compressor performed by Strazisar [28] in the Lewis research center. Furthermore, the S-duct is coupled with Stage 67B to analyze the effect of BLI on the performance of Rotor. An artificial neural network curve fitting-based surrogate model is used to optimize Stage. Therefore, efficiency and total pressure ratio are the objective functions of the whole computational domain.

4.2 Case Study

4.2.1 Computational Domain and Blade Parameter

As shown in figure 1 the rotor and stator have clean inlet and outlet. The inlet is single times of rotor diameter in a clean case.

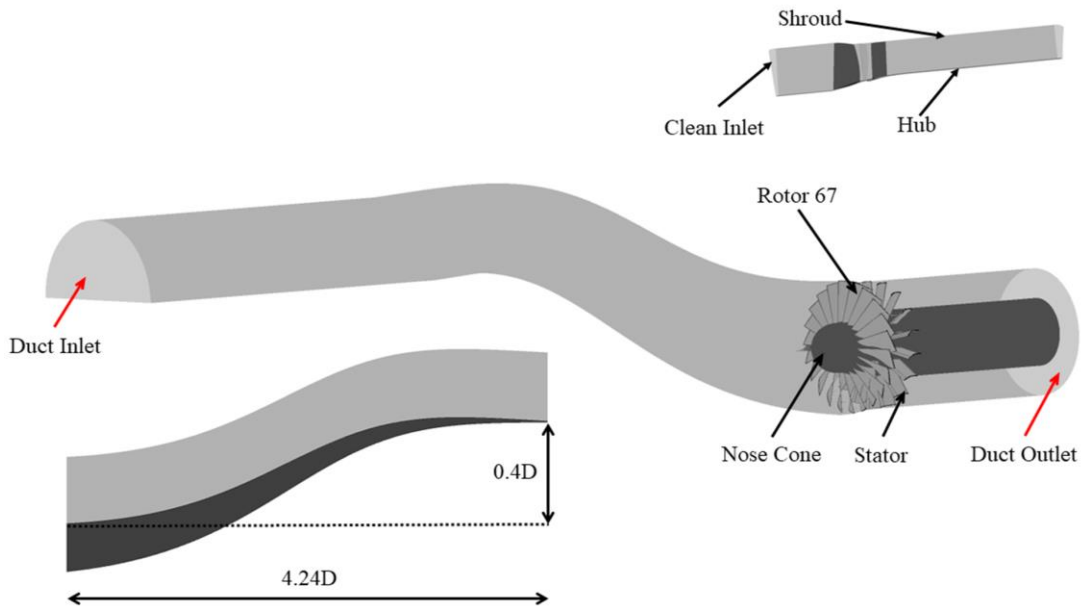


Figure 4.1 Representation of computational domain s-duct and NASA rotor 67

As the outlet is 1.5 times the diameter of stator outlet is used for validation and as a clean case without s duct [29]. Fig. 4.1 shows that Stage 67b is coupled with duct. The duct inlet is 3.8 times the diameter of rotor blade, it helps to grow boundary layer properly in a duct that approaches the fan face. The duct is model in SolidWorks used as inlet [30], [31]. As the rotor inlet is very short it is at the exit of duct outlet and the distance between the rotor and stator is same as defined by Thomas F [32]. Therefore, the outlet duct at the stator exit interface helps to stabilize the flow and to increase the convergence of the solution. The rotor used in this study is Transonic fan R67 along with the stator 67b [28]. The rotor solidity is 3.114 at hub and 1.29 at the tip. The hub tip ratio changes from 0.375 at inlet to 0.478 at outlet. The stator has 17 blades with double circular arc design [32]. The inlet to outlet hub to tip ratio is 0.5 to 0.53. More information is to be found in **Table 4.1** [33].

Table 4.1 Blade parameter of NASA stage 67B

Blade Parameters	Rotor	Stator
Total Number of Blade	22	17
RPM	16043	-
Pressure Ratio	1.63	-
Midspan Flow Coefficient	0.65	-
Load Coefficient	0.5	-
Aspect Ratio	1.56	2.01
Mean Hub to Tip Ratio	0.43	0.53
Blade Diameter [cm]	0.51	0.49
Isentropic Efficiency	92	-
Tip Mach Number	1.38	-

4.2.3 Grid Processing and Sensitivity Analysis

A Commercial software, Ansys Turbogrid, is used to generate multiblock structural grids. The H and O grid mesh is generated around the blade surface [24],[25]. To select the appropriate mesh, three different meshes were executed. The total element of the second mesh is three times the previous mesh in a rotor passage. Therefore, the stator mesh is two times the previous mesh. This strategy is adopted to choose the appropriate mesh concerning the result or computational cost. The grid independence size in the

rotor passage contains the number elements 300000, 900000, and 2700000, whereas the stator passage contains 200000, 400000, and 800000 elements.

An unstructured grid is generated in a duct passage whose number of elements is 225000, 675000 and 2100000 elements. The grid independence is computed against the total pressure ratio (TPR) and temperature ratio (TTR), as shown in Fig 4.2 (a,b).

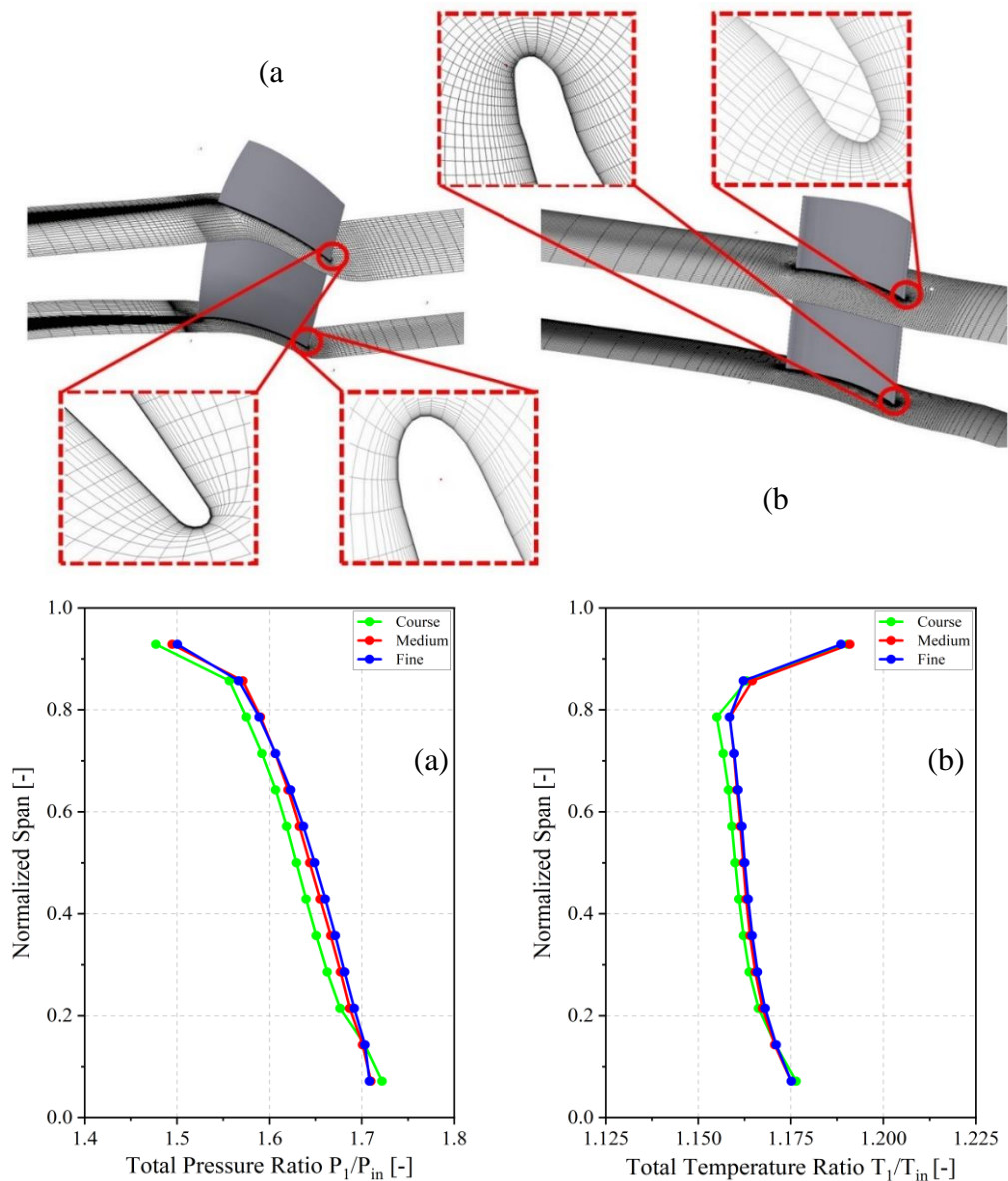


Figure 4.2 Representation grid around rotor and stator blade normalized span

4.2.3 Solver Setup

A steady state analysis was performed by Ansys CFX. Several turbulence models were available, like k epsilon, RNG, k omega, and SST. The best linear and nonlinear Turbulence model is RNG k-epsilon to account for the small motion near the blade

with the scalable wall function [36]. This is the modified model of the standard k-epsilon model. An Axisymmetric flow is considered in a single passage without a duct. The Adjacent side of the passage is treated as periodically. The single passages were simulated for solver validation against the experimental. The inlet static pressure is 101325 Pa with a turbulence intensity of 5%, and the inlet temperature is 288.15 K. The rotor and stator interface are set to be a mixing plane circumferentially averaging the velocity, pressure, and temperature [35]. The outlet is set to be a static pressure to increase the stability of the solution, which is gradually increased from choked to stall to compare the compressor map with experimentation.

To conclude, the effect of BLI on the fan's performance, thus s-duct, is coupled with the stage. The side-to-side interface of the whole annulus passage is a frozen rotor. Therefore, the remaining conditions are the same. The nose cone is attached within a duct that rotates in the direction of the blade at the same angular velocity. The lower surface of the duct acts as an adiabatic wall, while the upper surface acts as a free-slip wall. The inlet pressure is 101325 Pa at the duct inlet, while the interface is a frozen rotor between the duct outlet and stage. The outlet pressure is applied at the stator exit duct. The simulation was performed from the choke point to the stall point.

To conclude, the effect of BLI on the fan's performance, thus s-duct, is coupled with the stage. The side-to-side interface of the whole annulus passage is a frozen rotor. Therefore, the remaining conditions are the same. The nose cone is attached within a duct that rotates in the direction of the blade at the same angular velocity. The lower surface of the duct acts as an adiabatic wall.

4.3 Optimization Methodology

A multi-objective genetic algorithm optimization (MOGA) tool is used to optimize the trailing edge of the rotor, to improve the efficiency of the whole system by reducing the rotor and stator losses. After the compressor map validation, a baseline is simulated to analyze the losses that help to select the parameter in optimization. The design of the experiment is built by adopting the Box Behnken methodology.

All the experiments in DOE were simulated at a constant normalized mass flow rate. The surrogate model is developed using the artificial neural network (Ann). The mathematical model of Ann was read in the MOGA that generates the Pareto front by changing the dataset to a desired limit. The selected optimization point is tested using

the CFD analysis, concluding the difference between them. The whole methodology of validation and optimization is described in **Fig. 4.3**.

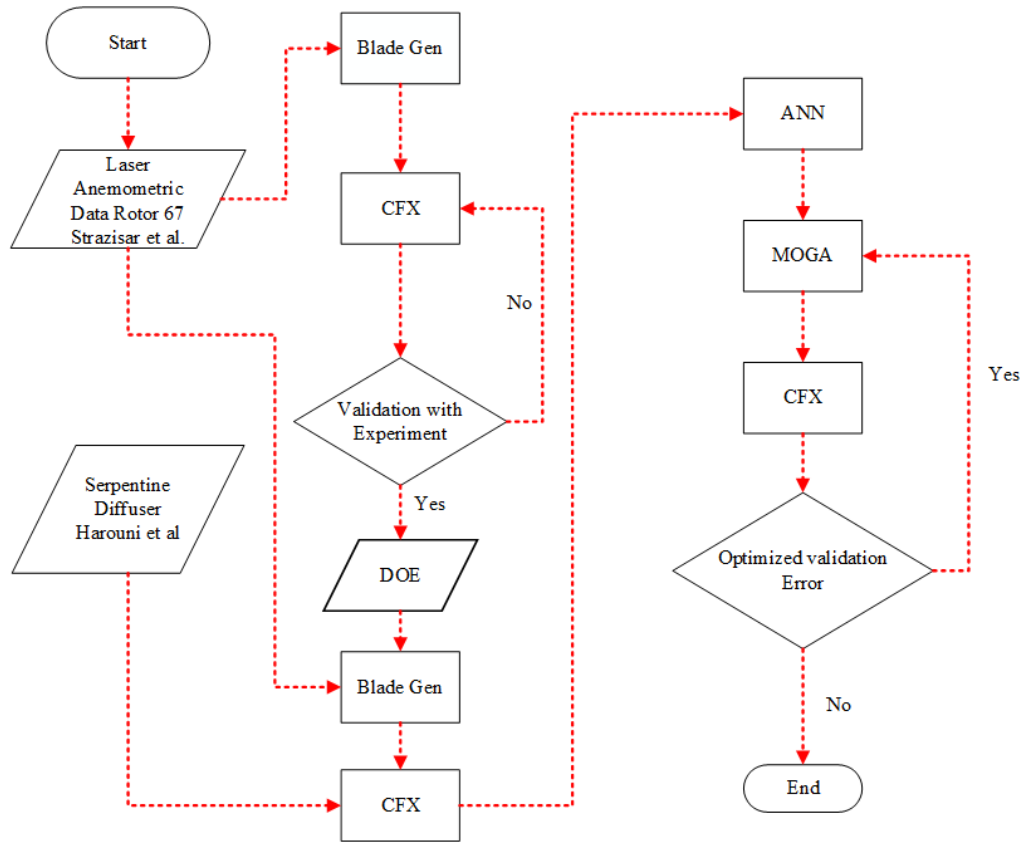


Figure 4.3 Methodology adopted for optimization.

4.3.1 Box Behnken Design (BBD)

The large-size problem required a huge computational power to figure out the results of the objective function. The design of the experiment approach is adopted to circumvent this problem to generate a surface response [37].

Table 4.2 Trailing edge parametrization bounds of the rotor blade

Input Variable	Blade angle	Bound
Blade angle, $\beta_{t.53}$	38.84°	$\pm 2.5^\circ$
Blade angle, $\beta_{t.76}$	50.66°	$\pm 2.5^\circ$
Blade angle, β_{t1}	54.42°	$\pm 2.5^\circ$

A BBD gives a higher-order surface response with fewer runs. It is a class of rotatable second-order design. The number of DOEs is generated based on $N=2k(k-1) + C_0$.

(Where k is the number of factors and C_o is the number of central points on the face). In this research, DOE is generated using three trailing edge points of the blade at different span locations. All the experiments in DOE is simulated approximately at the same normalized mass. The tolerance between the normalized mass in the experiment is ± 0.0005 .

4.3.2 Surrogate Model

The surrogate model was built based on high-fidelity simulation results obtained from the design of experiment (DOE). This model helps in the prediction of the mathematical model, which saves a lot of time and computation costs. Various surrogate models predict the mathematical model, like artificial neural network kriging, gradient-enhanced kriging, and polynomial response surface. This study selected the artificial neural network-based surrogate model for the mathematical model. There are two hidden layers in the ANN model. There is a total 10 number of neurons. Three neurons were in the first layer. At the same time, the remaining seven neurons were found in the second layer. The training is done by Levenberg Marquardt and is used to solve non-linear least-squared problems. The mean square error is 0.0047, and the value of R-squared is 0.99, which is slightly overfit due to the system's complexity.

4.3.3 Multi-Objective Optimization

Several optimization methods were extensively available in MATLAB, like the least squared method, Genetic algorithm, constrained nonlinear minimization, and multi-objective genetic algorithm (MOGA). Isentropic efficiency (η) and total pressure ratio (TRR) are the main objectives for optimization under the influence of BLI. The optimization is performed based on a mathematical model generated by Ann that reads in MOGA. Which is furthermore based on the biological process of generation.

Summary

To conclude, the effect of BLI on the fan's performance, thus s-duct, is coupled with the stage. The medium-type mesh is selected for the validation. The inlet temperature is 288.15 K with an inlet pressure of 101325Pa. The side-to-side interface of the whole annulus passage is a frozen rotor. Therefore, the remaining conditions are the same. The nose cone is attached to a duct that rotates in the direction of the blade at the same angular velocity.

Chapter 5 Results and Discussion

5.1 Validation

To validate the fan stage and computational setting, a single passage steady state analysis was performed at 100% Speed line to compare the CFD compressor map with the experiment performed by [18]. There is a very slight difference between the stall point and choke point.

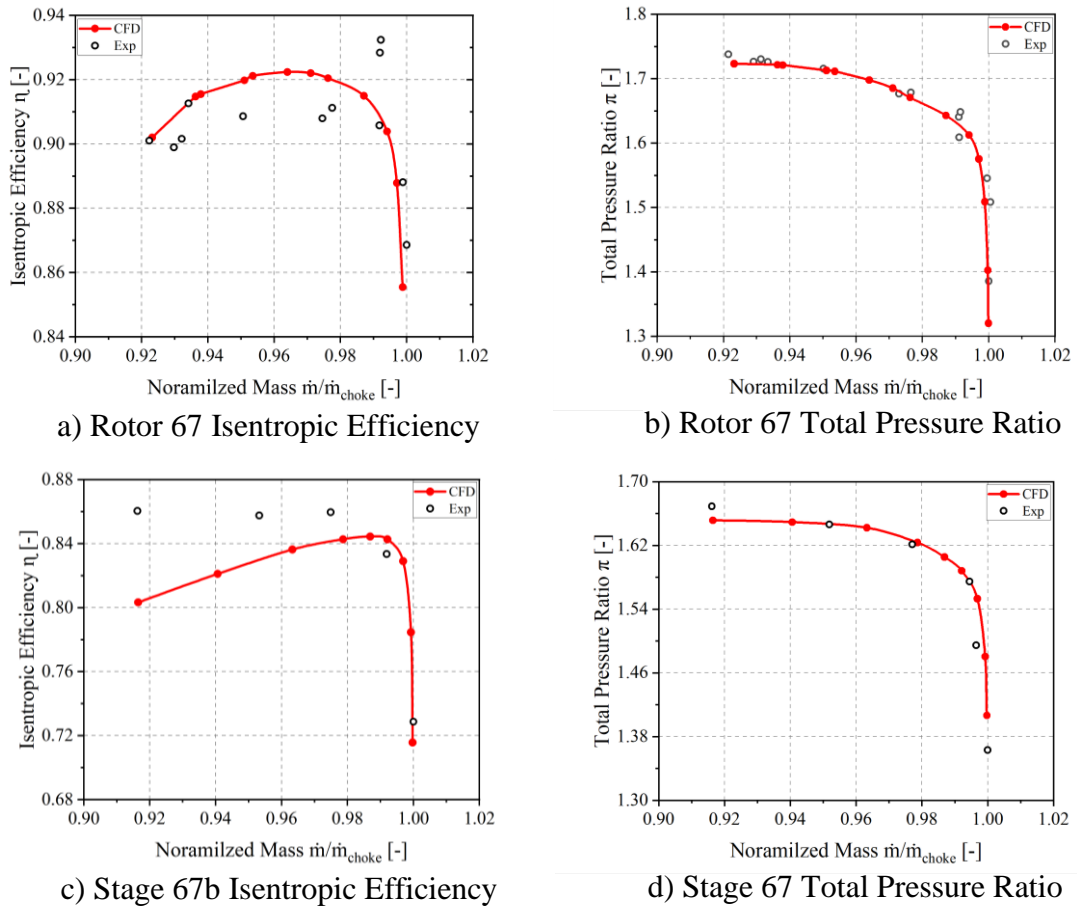


Figure 5.1 Validation of transonic fan NASA rotor 67 and stage 67B

The experimental maximum isentropic efficiency (η) and total pressure ratio (TPR) are 0.93 and 1.64. Hence, the maximum is η predicted by simulation is 0.9220, with a TPR of 1.6852. There is a very slight difference between them due to the minor change in velocity triangles [8]. There is a slight decrease in mass flow rate from a choke point, and there is a drastic increase in efficiency till the design point, but TPR increases till the stall point. As demonstrated in **Fig. 5.1**

5.2 Baseline Case Stage Flow Field

5.2.1 Fan Face Flow Field

As flow reaches the fan face, it is no longer axisymmetric in each sector. A circumferential distortion occurs in swirl angle, axial velocity, and incidence angle. A fan is operating at design speed instead of operating at the design point. The pressure and mass flow distribution are no longer uniform upstream of the fan. Due to the non-uniform circumferential distribution of inlet static pressure in the entire annulus, radial transportation occurs at the same plane near the fan face.

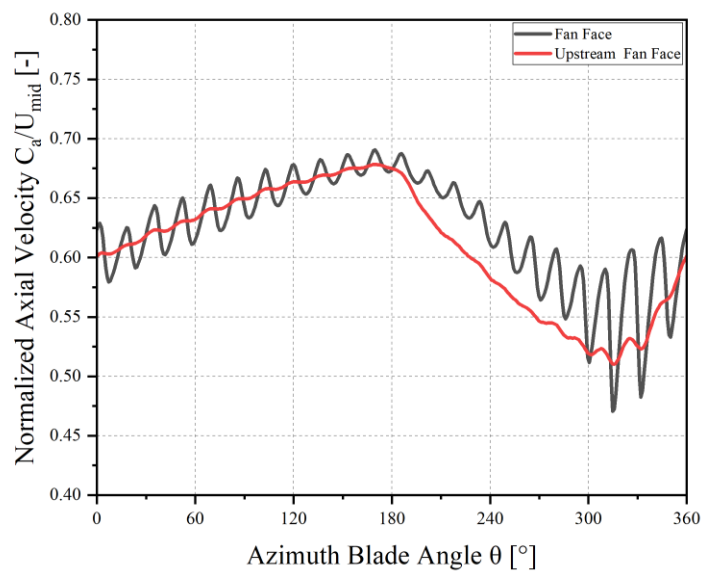


Figure 5.2 Normalized axial velocity at fan upstream and fan face

As the flow approaches the presence of the fan, its non-uniformities in axial velocity increase circumferentially, as shown in **Fig. 5.2**. Therefore, the same behavior in static pressure occurred at the fan face, affecting the radial flow distribution. As a result of flow distribution, it generates a co-swirl and counter-swirl, as described in **Fig. 5.3 (d)**. The radial flow distribution also occurs due to the presence of a spinner. The flow moves around the spinner in a radial direction, generating the swirl. Its intensity decreases as it moves from the hub to the tip. The maximum difference in flow occurs at 160° , where the direction of the counter swirl changes to co-swirl and starts decreasing. In the upper half region of annulars, the pressure is high at the fan upstream, while the flow tends to move from a region of higher pressure to lower pressure around a nose cone, as represented in **Fig 5.3 (b)**.

The stagnation point lies at the blade center in the absence of a nose cone. Hence, in the presence of the nose cone, the stagnation point lies at the bottom of the blade near the region of cleaner flow. The fan tries to recover this mass flow deficit. The region of lower mass flow rate that shows the fan working the at stall point gives slightly higher pressure, while the region of higher mass flow rate means the fan working near the choke point gives lower static pressure and higher efficiency. Static pressure gives a brief idea about the region where the isentropic efficiency drops and increases. It further depends upon the incidence angle.

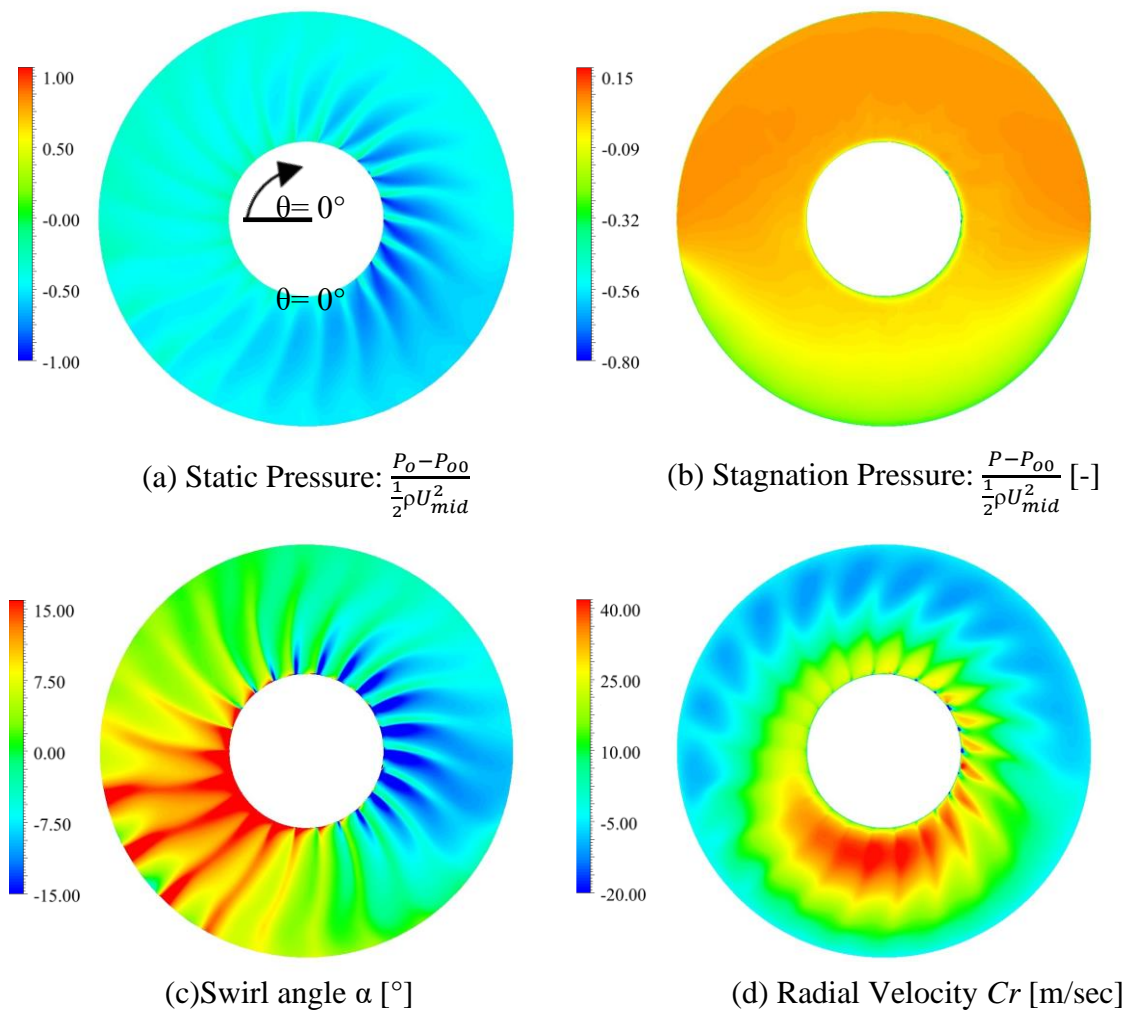


Figure 5.3 Non-uniformities at fan face in static pressure, stagnation pressure, swirl angle, radial velocity

Incidence angle is highly dependent upon the swirl angle and axial velocity. As the swirl angle starts decreasing, it causes an increase in the axial velocity described in Meanwhile, both combine to decide the final incidence angle. **Fig 5.4 (b)** Indicates

that the swirl angle drops from hub to tip due to radial fluid transportation around the spinner. As the swirl angle drops from a higher positive angle to a negative, the incidence angle starts increasing from lower positive to higher values, as represented in **Fig 5.4 (c)**, causing an increase in the intensity of the counter swirl from 0 to 180°. The black line indicates that the region near the hub has a maximum strength of counter-swirl at 180°. The maximum difference in swirl angle occurs at 180° that shows the region of the higher counter swirl will be slowly changed to co-swirl but behaves as counter co-swirl from (180-270°). The intensity drops continuously till 270°. The dark blue line indicates low-intensity counter swirls in whole annuals near the tip. The region (270-0°) will suffer the most due to a higher positive swirl angle and low axial velocity.

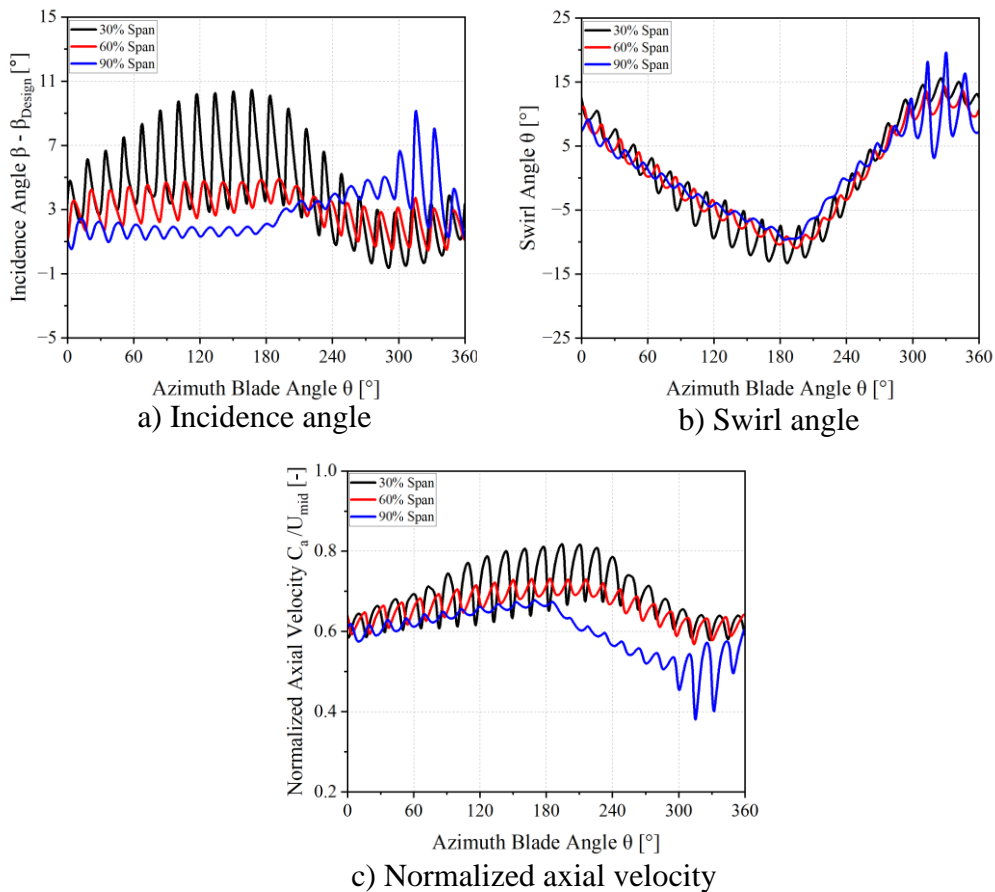


Figure 5.4 Fan face distortion in incidence angle, normalized axial velocity and swirl angle at 30%span, 60%span, and 90%span.

5.2.2 Rotor Flow Field

As the Flow Passes through a blade passage, its axial velocity increases, as shown in **Fig 5.5 (a)**. The increase in axial velocity is maximum near the hub at 180° due to a significant decrease in counter-swirl. Its axial velocity drop (270° - 360°) increases the flow separation due to high static pressure at the fan face. This area (270° - 360°) near the tip suffers the most, reducing the whole performance of the fan.

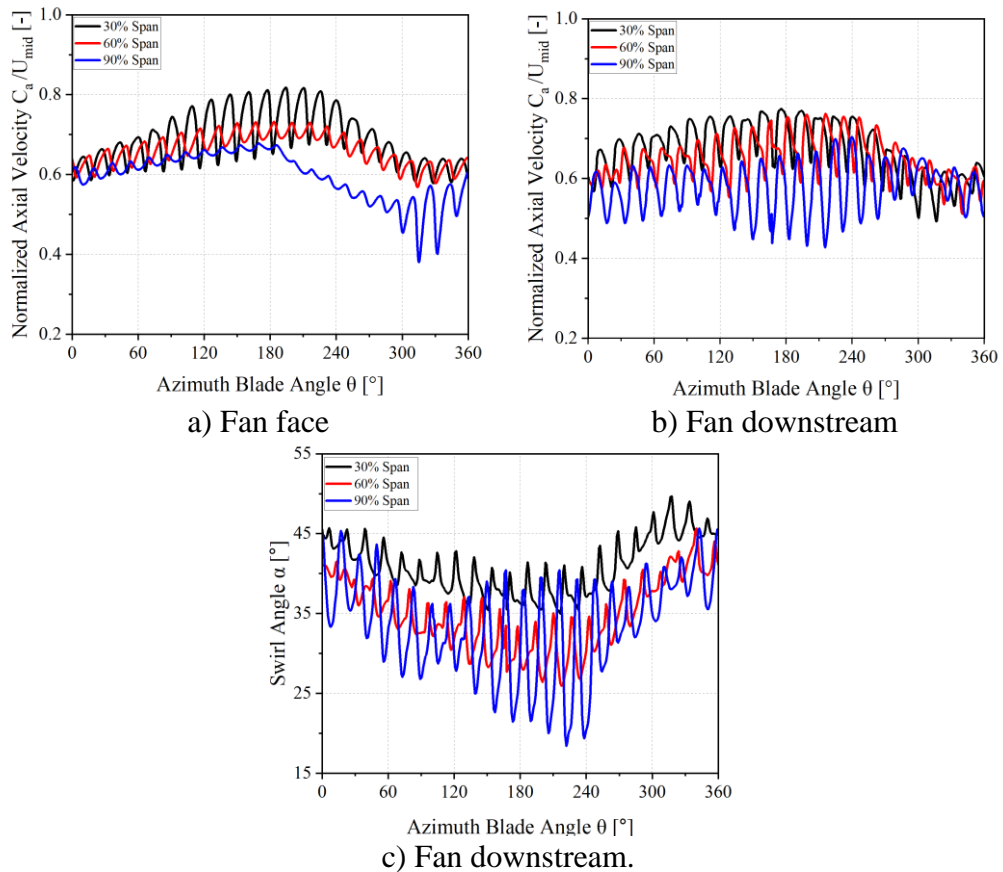


Figure 5.5 Swirl angle and normalized axial velocity at rotor exit

The temperature ratio (TR) gives an insightful idea about the fan's work input, as represented in **Fig 5.5 (b)**. Due to inlet distortion inflow at the fan face, there is also some non-uniformity in TTR. The increase in TTR was observed near the hub and casing of the fan. As the fan passes through the region of high counter-swirling (0 - 180°), it starts increasing near the hub due to a positive drop in swirl angle and an

increase in axial velocity, causing an increase in the incidence angle from negative to positive as a result TTR efficiency increased.

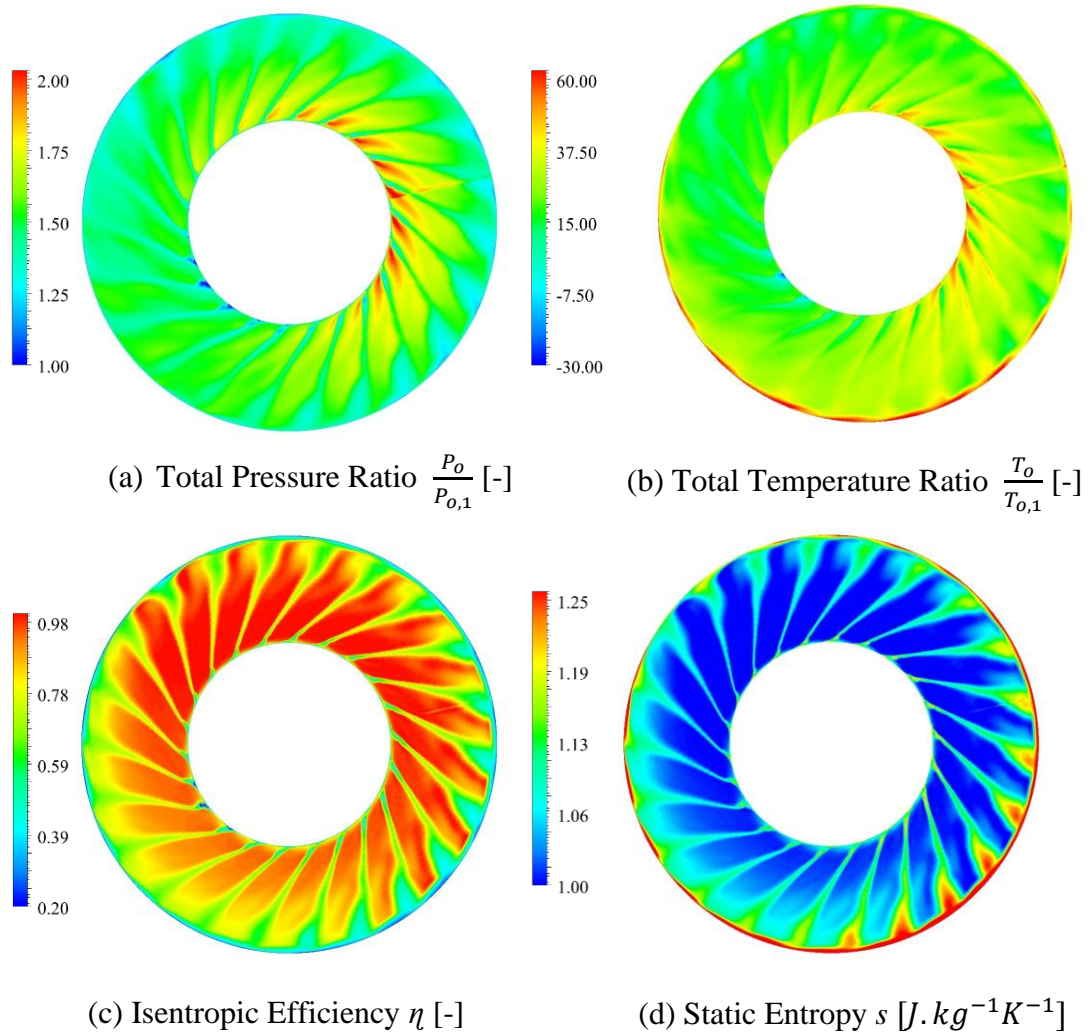


Figure 5.6 Rotor downstream face contour

TTR will be maximum at the end of the counter-swirling region at 180. After that, it starts decreasing and becomes the minimum near the hub at 0° due to the high negative value of the incidence angle. The tip area is working at the region of strong contour swirl region at the fan face, as described in **Fig 5.6 (c)**, causing an increase in the TR. Therefore, the same behavior is observed in a Total pressure ratio (TPR). The areas with a greater temperature ratio have higher TPR and vice versa. However, they have

a lower TPR toward the casing because the viscous layer near the casing wall tends to mix with the mainstream flow.

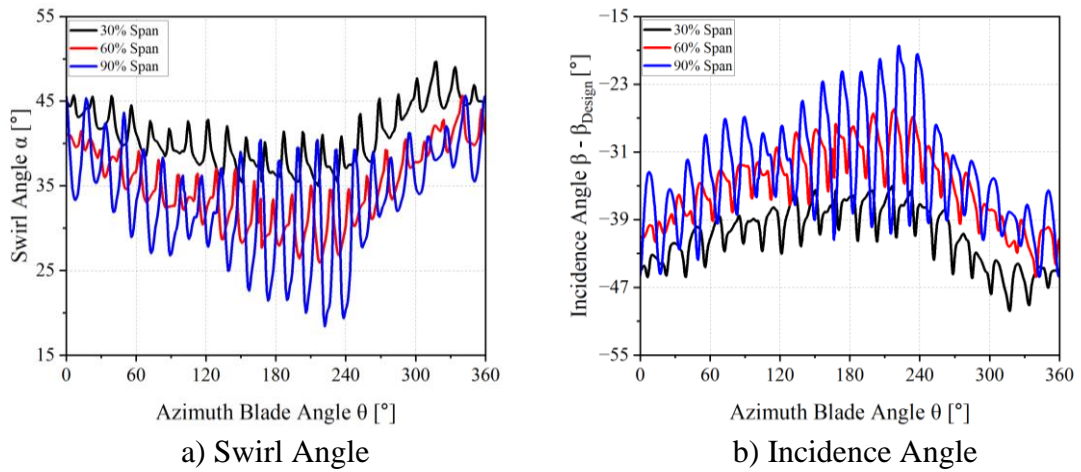


Figure 5.7 Swirl angle at stator face and incidence angle

Static entropy (s) directly relates to the losses that occur in a region. S increased from hub to tip and became maximum near the tip. The region where the static entropy is high has a significant drop in isentropic efficiency and is tolerated the most in a whole system. TPR decreases near the casing as the flow passes through a shock wave, causing flow separation. The boundary layers of lower energized fluid thickened the viscous layer near the casing due to an adverse pressure gradient. When it detaches from the casing, this boundary layer mixes with the mainstream flow causing increased losses. Hence, the entropy increases near the tip, as illustrated in **Fig. 5.6 (d)**.

5.2.3 Stator Flow Field

The extra gained energy from the fluid by the rotation of the rotor is affected in a stator passage, which results in a series of non-uniformity in swirl flow. The distorted flow approaches the guide vanes, and the overall performance of the stator decreases due to the highly negative incidence angle (θ°) near the hub described in **Fig 5.7 (b)**. The performance of the region ($0 - 180^\circ$) improves when the swirl angle starts to move from positive to negative in magnitude, while the opposite is true for the incidence angle. Therefore, the region ($270-360^\circ$) overall performance is tolerated near the tip and hub by the manifestation of co-swirl and highly negative incidence angle that increases the flow separation near the hub and tip.

Fig. 5.8 shows that when a flow transverses through the stator, its aerodynamic losses are evident at the side-by-side periodic interfaces near the hub caused by the highly positive swirl angle that increases the flow separation. These losses tend to reduce the work input of the stator due to increased static entropy near the hub and shroud wall, reducing the isentropic efficiency and the temperature drop. As can be seen, there is a performance drop at a particular region ($270 - 360^\circ$) owing to variation in incidence angle from a lower negative value to a higher negative value. As explained above, a significant drop in efficiency is observed near the hub be (see Fig. 5.8).

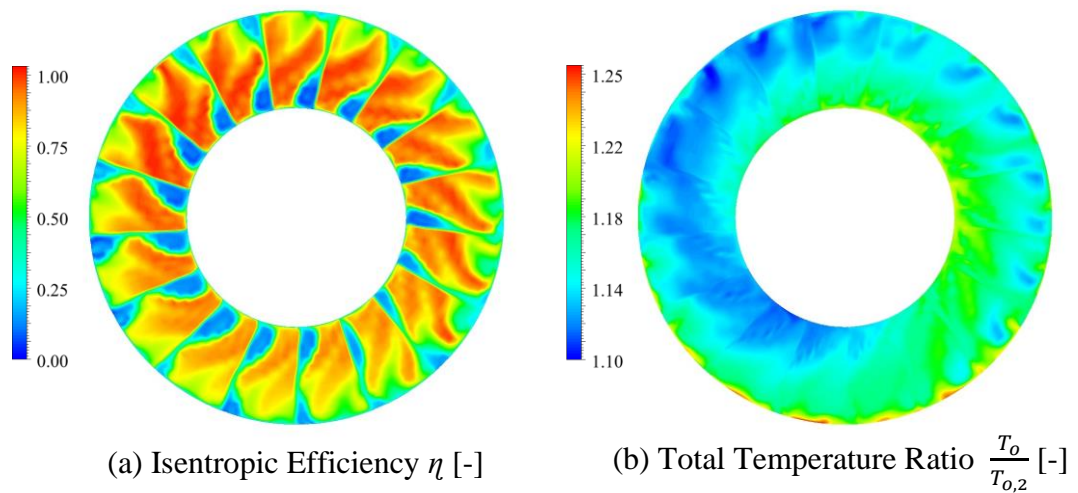


Figure 5.8 isentropic efficiency and Total temperature ratio at stator downstream

5.3 DOE-Based Baseline Optimized Test

Ann developed surrogate-based mathematical based on DOE. The value of r-squared represents the curve fitting of the mathematical model. The higher the value of r-squared, the greater the curve fitting of the model that presents the accuracy of the whole system. The value of R-squared is 0.99 with a root mean square error of 0.004, slightly over fit due to the complexity of the entire system. The mathematical model is simulated on MATLAB using MOGA that optimizes both the isentropic efficiency (IE) and total pressure ratio, as shown in **Fig 5.9**.

The selected point is validated by using the CFD simulation. The result shows that the deviation between IE is greater than MOGA due to the slight over fitness of the mathematical model. Therefore, another reason behind them is the complexity and size

of the whole system. Moreover, a significant increase is observed in the optimized case compared to the baseline, as discussed in section 4.3.

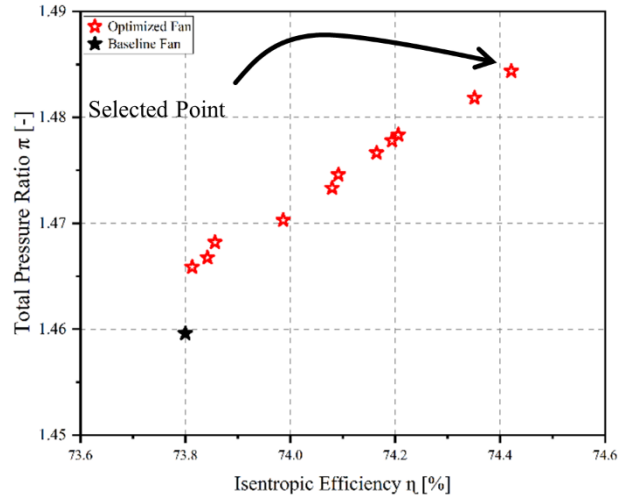


Figure 5.9 Pareto front of optimized blade

Table 5.1 Comparison of objective functions

Objective Function	MOGA	CFD	Deviation [%]
Total Pressure Ratio	1.4884	1.4842	0.28
Isentropic Efficiency [%]	74.42	75.95	2.1

5.4 Optimized Case Rotor Flow Field

5.4.1 Fan Face Flow Field

The three trailing edges of the rotor are optimized at 50% span, 70% span, and 100% span. To improve the aerodynamic properties near the tip. **Fig 5.10** Clearly describes the optimized blade did not have the same behavior as the baseline case except for normalized axial velocity swirl angle.

The non-uniformity in inlet distortion in normalized axial velocity, swirl angle, and incidence angle is minor reduced at the fan face near the tip due to shock wave penetration into the leading edges of the adjacent blade. Three different cases studied in this portion were discussed: Without (W/O) duct case, also called a clean case, a baseline case, and an optimized case. A clean case presents the effect of clean inlet flow without a duct on the fan's performance, while a baseline case studies the effect of BLI. However, the optimized case discusses the flow field that improved due to optimization under the influence of BLI.

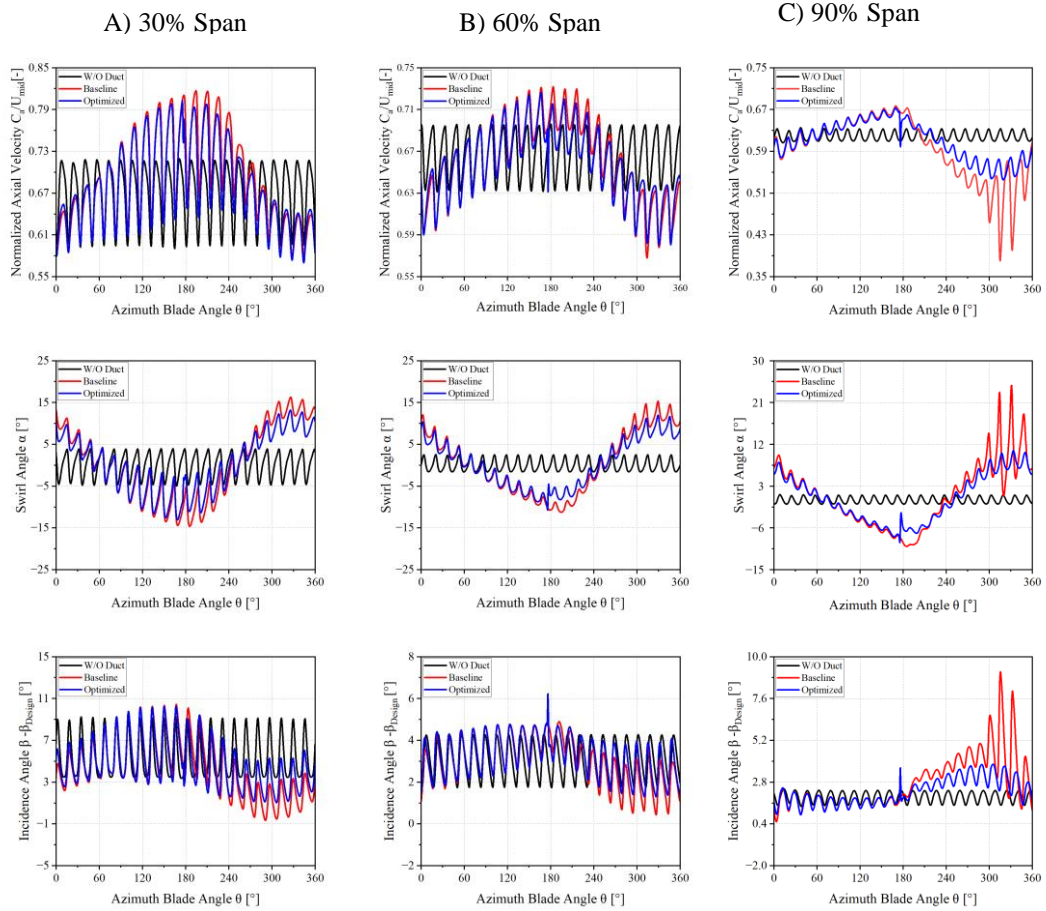


Figure 5.10 Comparison of baseline and optimized flow field

The flow field in an optimized case is fully non-uniform over the fan face as the baseline case. An increase in axial velocity is significant in a region (180-360°) near the tip that affects the whole aerodynamic performance of the blade due to the slight reduction in boundary layer induced at the blade's tip that affects the swirl angle. Moreover, the swirl angle is almost the same as the baseline except near the tip from (300-360°) due to constant static pressure. The incidence angle is the function of normalized axial velocity and swirl angle. As the incidence angle increases from lower positive to higher, the intensity of the counter swirl increases, which improves the aerodynamic performance. A major improvement occurs in an incidence angle (180-360°) due to the reduction in axial velocity.

5.4.2 Optimized Rotor Flow Field

Fig 5.11 (a) Present total temperature ratio (TTR) comparison of baseline case and optimized case. The TTR is non-axis symmetrically distributed over the downstream

of the rotor. Therefore, TTR increases (0-90°)-(270-360°) from hub to tip due to increased axial velocity.

The incidence angle remains the same as the baseline case. The mid-span of the blade from the hub due to a lack of improvement in swirl angle and normalized axial velocity. Moreover, at the tip incidence angle, it moves toward the region of an undistorted flow like a W/O duct case, and as a result, its flow separation is reduced at the blade wall, causing to an increase in the TTR.

Fig 5.11 (c) clearly shows the decrease in static entropy to (0-90°)-(270-360°) from hub to tip as a result of an increase in TPR. The positive gain in isentropic efficiency (η) at downstream of the rotor is caused by the radially circumferential increase in incidence angle. Thus, its η slightly drops near the hub (90-180°) due to the slight decrease in the axial velocity. The increases η evenly distributed in the radial direction in a whole circumference led to a reduction in the static entropy (s). The overall decrease in s average is 5.2%, and the increase in η at the rotor downstream by 2.11%, the average increase in TTR is .18%.

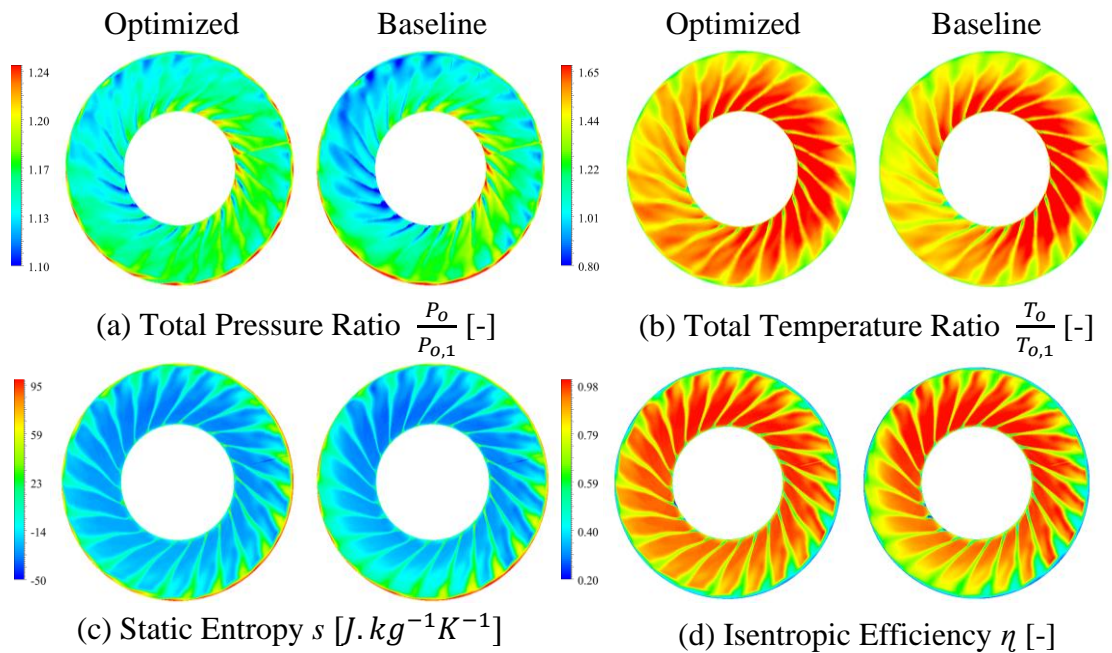


Figure 5.11 Optimized and baseline contour comparison.

The overall improvement is clearly described in **Fig 5.11** as a result of optimization. As the flow passes through the fan, its swirl angle shifts from a higher positive to a lower value due to work input done by the fan on flow. As in the optimized case, the total pressure ratio (TPR) is maximum near the blade's tip due to the significant

increase in the axial velocity and swirl angle caused by the reduction in boundary flow separation between the walls of the blade in optimization. Moreover, the effect of the trailing edge also occurred at the hub section. The swirl angle improves near the hub, causing an increase in the TPR (0-60°) - (300-360°) at a 30% span. While at 60% span, the increase in TPR is more uniformly distributed-circumferentially due to a positive decrease in a swirl angle.

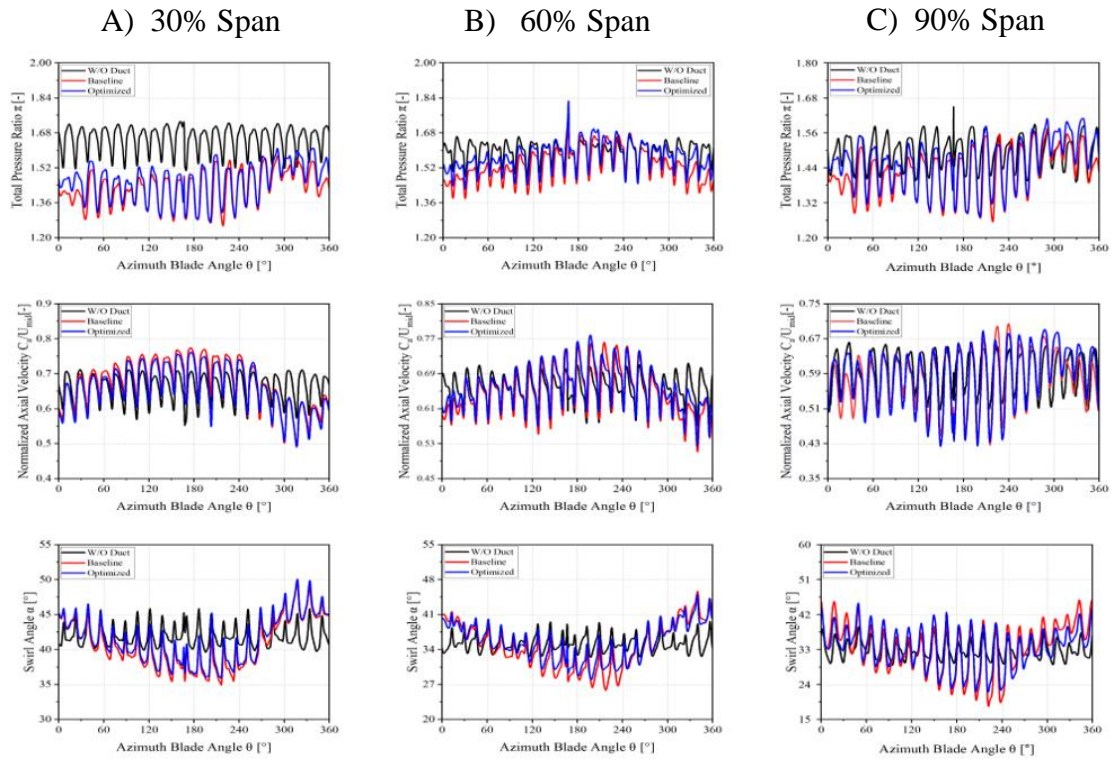


Figure 5.12 Optimized Total pressure ratio normalized axial velocity and swirl angle compared to baseline at 30%span, 60%span and 90%span

The TPR is on average improved by 1.177 % due to the increase in axial velocity by 1.9152%, reducing the flow separation at the rotor downstream. The increased swirl angle also manifested, which helped to improve the incidence angle at the stator face. The swirl angle is improved by 5.45%, directly affecting the isentropic efficiency at the downstream rotor. The static entropy drops by 5.266% with the increases of static enthalpy by 4.5%, directly impacting isentropic efficiency. Therefore, isentropic efficiency increases by 2.11% due to a drop in static entropy. The shock waves

improving the tip section is the main reason, as explained in the section blade-to-blade comparison.

5.4.3 Optimized Case Stator Flow Field at Downstream Face

Fig. 5.13 represents the comparison of baseline and optimized stator exit. A rise in temperature at the stator exit was observed near the tip due to reduced wake generated around the stator blade. However, the region (270°-360°) tolerates inevitably due to very high fluctuations in co-swirl and low normalized axial velocity (270-360°) in the baseline case. Therefore, in the optimized case, both decrease near the clean flow. As a result, aerodynamic performance increases in terms of flow separation due to an increase in normalized axial velocity near the tip. Here, the decrease in axial velocity near the hub causes a reduction in incidence angle from a higher negative to a low negative, causing a drop in the total temperature ratio (TTR), as shown in the red dotted line in Fig 5.13 (b).

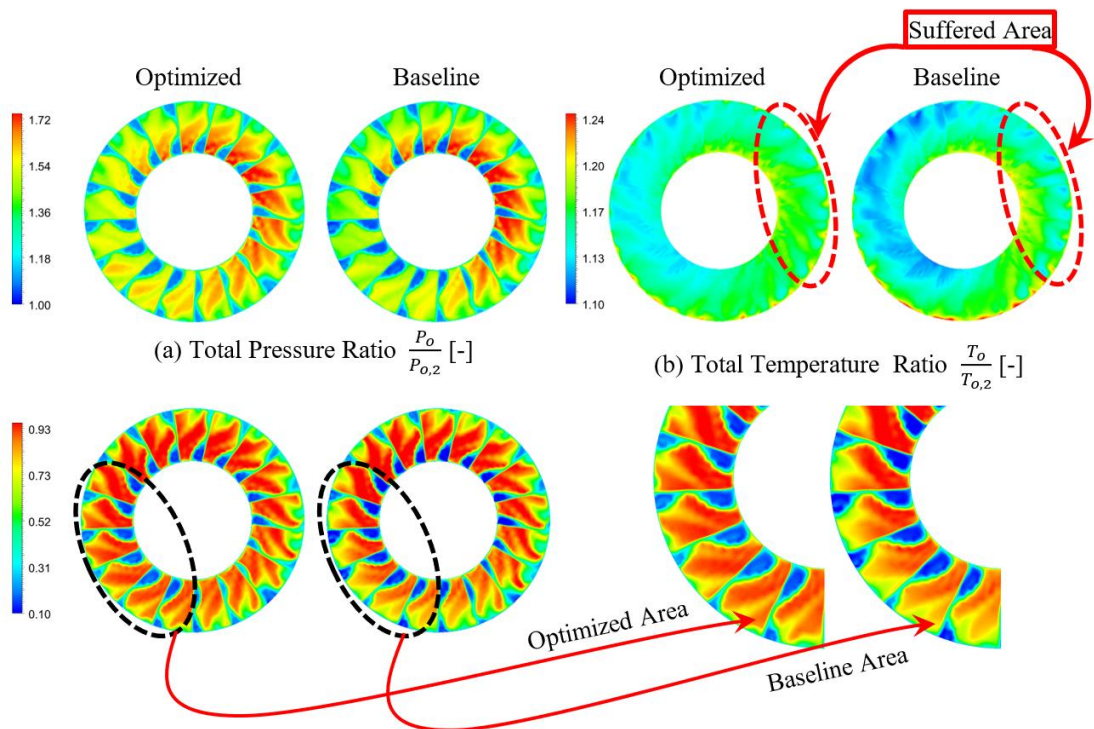


Figure 5. 13 Optimized and baseline contour comparison at stator downstream

The total pressure ratio (TPR) started increasing near the hub at a 30% span (270-360°). In this region, a pure co-swirl that lies in the baseline case due to variation induced in static pressure at the rotor downstream, the maximum increase in TPR is observed as a result of optimization near the hub from (270-360°).

The increase in normalized axial velocity in tandem with the positive increase in swirl angle reduces the stator losses. Meanwhile, the high counter swirl region also decreases near the hub from (60-210°) due to a drop in incidence angle at the stator face near the hub. The incidence angle is the function of normalized axial velocity and swirl angle. Due to decreased normalized axial velocity at the fan face, the incidence angle drops at the stator face at the middle of the blade (60-270°).

Therefore, it is clearly shown in Fig. 17 that the baseline isentropic efficiency (η) drop is maximum across the hub and tip of the stator at each periodic interface. As the flow transverses through the stator with an increased axial velocity, its flow separation is overcome due to a lower positive swirl angle along with a lack of radial flow in the passage that occurs due to the slight increase in static pressure at the tip. The normalized axial velocity increased maximum near the tip at 90% span, reduced the flow turning due to improvement in swirl angle is maximum (270-360°), and increased in the incidence angle at the fan face, causing an increase in the η , as represented in a black dotted region as shown in **Fig 5.13 (d)**.

As its axial velocity tolerates slightly away from the hub, a 30% span (60° to 240°) inevitably leads to a decrease in the isentropic efficiency due to the reduction in static entropy. Conversely, there is flow separation near the hub due to a higher negative incidence angle at the wall, causing a drop in the isentropic efficiency. At 60% span, axial velocity increased, yet there was no flow separation due to a lower negative incidence angle. Higher normalized axial velocity and swirl angle are helpful to maintain the positive incidence angle at mid-span at the stator face. The optimized incidence angle at 90% span starts to decrease from a higher negative angle to a lower negative value in the radial direction, which reduces the flow separation near the tip, causing to increase in the η .

5.4.4 Optimized Flow Field at Duct-Outlet.

As the flow moves from the stator downstream face, it revolves around the hub wall. Fig. 5.14 represents the improved flow field captured at the outlet. At 30% span, the flow field is slightly un-distorted due to a reduction in the intensity of counter-swirl (90-270°) along with the drop in axial velocity approaches to clean case (0-180°). As a result, the total pressure ratio (TPR) improved due to the decrease in intensity of co-swirl at the stator face in a whole passage. No further improvement is observed in the middle of the blade due to the lack of improvement in the incidence angle at the fan

face. Moreover, a dramatic change is kept at the blade's tip due to increased axial velocity near the clean flow in the without duct case.

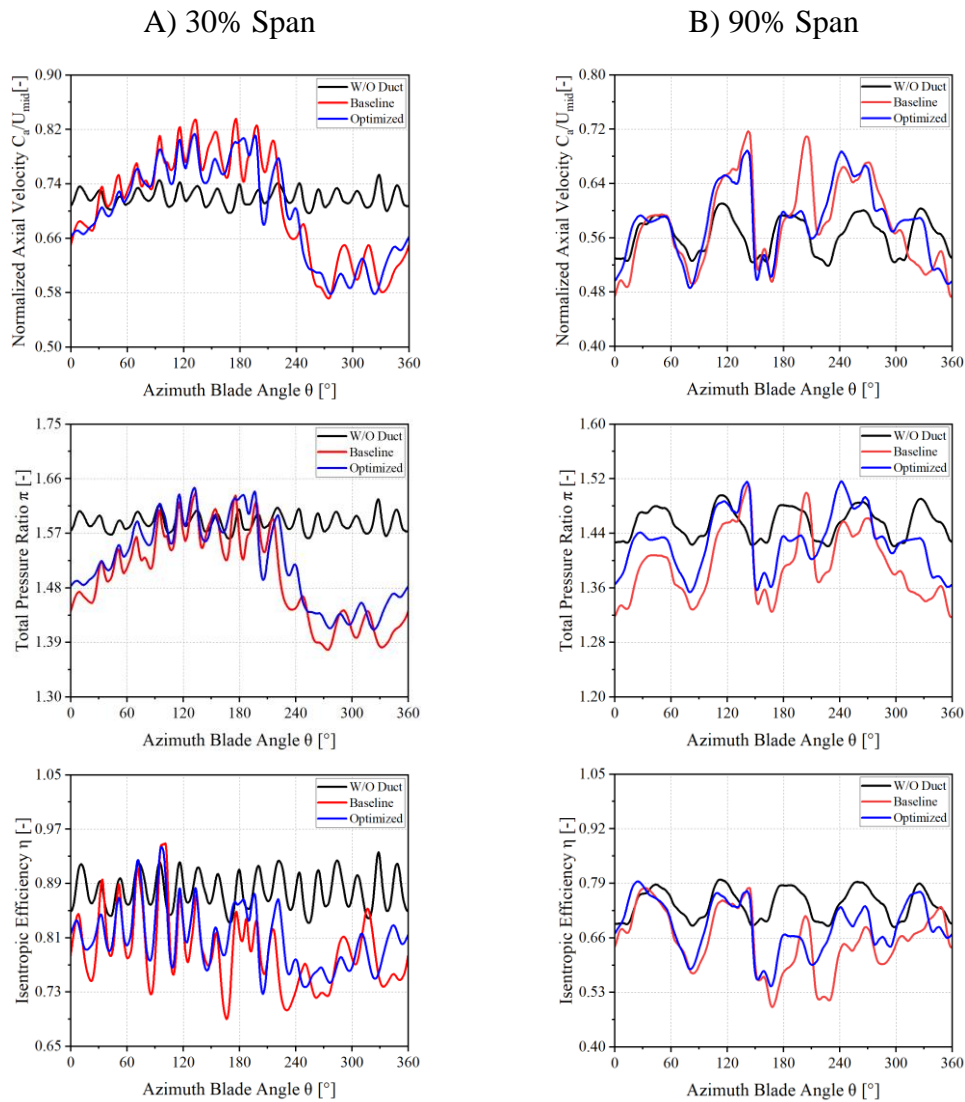


Figure 5.14 Isentropic efficiency total pressure ratio and normalized axial velocity contour comparison at duct downstream.

The isentropic efficiency of the system exhibited a noteworthy improvement, specifically increasing by 5.4%, coinciding with a concurrent reduction in static entropy by 3.32%. Furthermore, the overall pressure ratio experienced a notable augmentation of 2.06%, attributable to a proportional augmentation in the intensity of the swirl angle by 0.82%. These observed alterations in key parameters hold promise for advancing the efficiency of the entire gas turbine.

5.4.5 Blade to Blade Comparison:

Fig. 19. Present the blade-to-blade flow behavior of Mach number and Temperature ratio at 90% span. The un-distorted flow has a higher mass flow rate than the distorted flow. The distorted flow starts increasing near the green line from 180°. Furthermore, the black dotted oval in **Fig 5.15 (a)** represented area that most suffers under BLI due to highly distorted flow in the baseline. The location of the shock wave is highly dependent on the mass flow rate passing through each sector of the whole annulus. At a higher mass flow rate near the choke point, shock waves were entirely swallowed at the blade's trailing edge (90-180°). For the distorted flow (270-360°), shock waves moved upstream of the blade's leading edge, combined with the bow shocked waves near the leading edge, making a more substantial shock wave.

The shock waves are created close to the blade's trailing edge for the undistorted zone and interact with the pressure surface boundary layer of the adjacent blade, causing it to isolate. A significant wake can be visible downstream of the fan since the flow does not entirely reattach with the profile of the blades. The shock travels upstream as the blade passes through the distorted sector, generating flow separation on the blade suction surface. Therefore, in an optimized case, inevitable improvement is observed in shock waves being moved at the suction side of the blade, causing the flow separation to decrease. A noticeable improvement occurs at the incidence angle at the fan face, as discussed above.

Due to lower mass flow, TTR contours demonstrate that the fan works in the distorted sector. As the fan approaches the distorted sector, the counter swirl increases, enhancing the incidence angle and the work done. The TTR decreases when the fan comes to the clean sector. This is owing to high co-swirl levels, which limit the total work done. While, as a result of optimization, the intensity of co-swirl decreases along with a slight decrease in incidence, the work done tries to distribute over the surface uniformly.

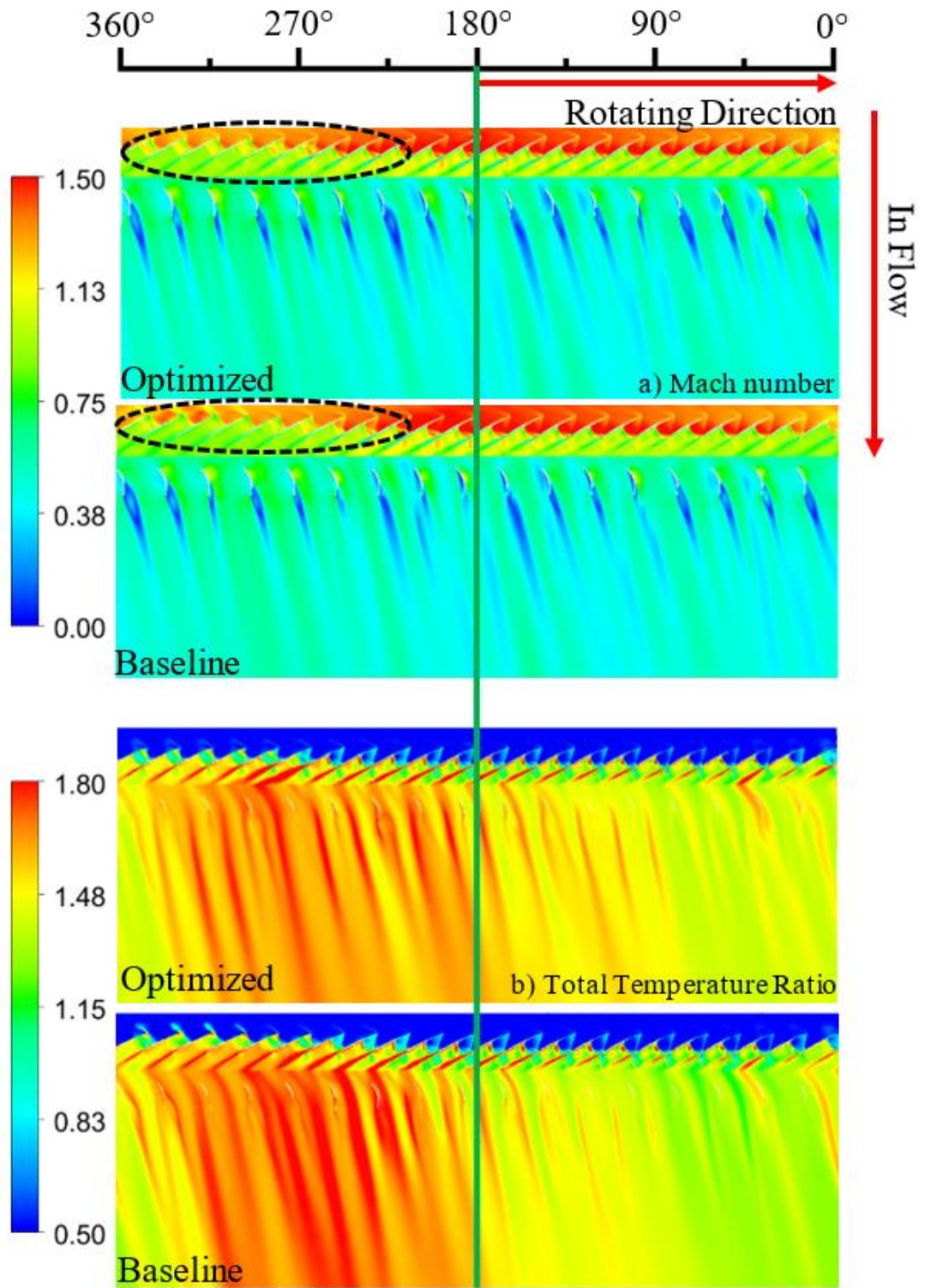


Figure 5.15 Blade to comparison of contour between optimized case and baseline with respect to Mach number and total temperature ratio at 90% span

Summary

As the flow passes through the fan, its swirl angle shifts from a higher positive to a lower value due to work input done by the fan on flow. As in the optimized case, the total pressure ratio (TPR) is maximum near the blade's tip due to the significant increase in the axial velocity and swirl angle caused by the reduction in boundary flow separation between the walls of the blade in optimization. Moreover, the effect of the trailing edge also occurred at the hub section. The swirl angle improves near the hub, causing an increase in the TPR (0-60°) - (300-360°) at a 30% span. While at 60% span, the increase in TPR is more uniformly distributed-circumferentially due to a positive decrease in a swirl angle. TPR is on average improved by 1.177 % due to the increase in axial velocity by 1.9152%, reducing the flow separation at the rotor downstream. The increased swirl angle also manifested, which helped to improve the incidence angle at the stator face. The swirl angle is improved by 5.45%, directly affecting the isentropic efficiency at the downstream rotor. The static entropy drops by 5.266% with the increases of static enthalpy by 4.5%, directly impacting isentropic efficiency. Therefore, isentropic efficiency increases by 2.11% due to a drop in static entropy. The shock waves improving the tip section is the main reason, as explained in the section blade-to-blade comparison.

Chapter 6 Conclusions and Recommendations

6.1 Conclusions

The Model NASA Stage 67 is validated against the experiment performed from the choke point to the stall point. A slight difference occurs between the compressor map due to a minor change in the velocity diagram. The S-duct is combined with a stage to study the effect of the boundary layer.

As the flow approaches the fan face, a non-axis-symmetric distortion occurs at each passage of the whole annulus. Due to inlet distortion, the Normalized axial velocity and swirl angle variation appear at the fan face. Meanwhile, the incidence angle is the function of normalized axial velocity and swirl angle. The co-swirl generated around the nose cone significantly affects the fan's performance. For the distorted flow, fan performance reduces as the intensity of the co-swirl increases. Moreover, for undistorted flow, the normalized axial velocity increases, and the swirl angle decreases as the intensity of the counter-swirl increases. As a result, the aerodynamic performance of the stage increases.

For a distorted region, the Inlet Mach number is less as compared to an un-distorted region. The shock wave moves upstream of the fan face leading edge and merges with the bow of the shock wave, becoming a strong shock wave caused to stall the fan and drop its isentropic efficiency. To reduce the losses around the stator and rotor, a trailing edge of the blade is parameterized at 55% span, 76%, and 100% to increase its performance. The isentropic efficiency and total pressure increase as a result of optimization. Co-swirl intensity decreases with the increased normalized axial velocity, which helps improve the incidence angle. Hence, the shock wave moves toward the trailing edge of the blade, causing an increase in the isentropic efficiency of the fan.

6.2 Future Prospects

This paper serves as a baseline to perform its high-fidelity unsteady simulation to capture the shock wave induced near the stall point to understand the flow field transiently. This paper presents the optimization of the blade, which can be extended

from baseline or optimization to improve the flow field around the stator to overcome the wave generated around the blade by parametrizing the flow angle of the 3-D blade.

References

- [1] I. Abrantes, A. F. Ferreira, A. Silva, and M. Costa, "Sustainable Aviation Fuels and Imminent Technologies - CO₂ emissions evolution towards 2050," *J Clean Prod*, vol. 313, Sep. 2021, doi: 10.1016/j.jclepro.2021.127937.
- [2] B. Graver, K. Zhang, and D. Rutherford, "CO₂ Emissions from Commercial Aviation, 2018," 2018.
- [3] "European aviation report 2019".
- [4] C. A. Hall, E. Schwartz, and J. I. Hileman, "Assessment of Technologies for the Silent Aircraft Initiative," *Journal of Propulsion and Power*, vol. 25, no. 6, pp. 1153–1162, 2009, doi: 10.2514/1.43079.
- [5] J. L. Felder, G. V Brown, H. D. Kim, and J. Chu, "Turboelectric Distributed Propulsion in a Hybrid Wing Body Aircraft," 2011.
- [6] M. A. Potsdam, M. A. Page, R. H. Liebeck, D. McDonnell, L. Aerospace, and C. Beach, "Blended Wing Body Analysis and Design*," 1997.
- [7] L. H. Smith, "Wake Ingestion Propulsion Benefit," *Journal of Propulsion and Power*, vol. 9, no. 1, pp. 74–82, 1993, doi: 10.2514/3.11487.
- [8] M. Burston, K. Ranasinghe, A. Gardi, V. Parezanović, R. Ajaj, and R. Sabatini, "Design Principles and Digital Control of Advanced Distributed Propulsion Systems," *Energy*, vol. 241, p. 122788, 2022, doi: <https://doi.org/10.1016/j.energy.2021.122788>.
- [9] T. Ben Sghaier, A. Mehdi, V. Pachidis, and D. MacManus, "A Parametric Numerical Study of the Effects of Inlet Swirl Distortion on a Transonic Compressor Stage," 2013. [Online]. Available: <http://www.asme.org/about-asme/terms-of-use>
- [10] A. Sieradzki, T. Kwiatkowski, M. G. Turner, and B. Łukasik, "Numerical Modeling and Design Challenges of Boundary Layer Ingesting Fans," *J Turbomach*, vol. 144, no. 11, Sep. 2022, doi: 10.1115/1.4055265.
- [11] W. Zhang and M. Vahdati, "Investigation of the tip injection for stall control in a transonic compressor with inlet distortion," *Journal of the Global Power and Propulsion Society*, vol. 5, pp. 28–38, 2021, doi: 10.33737/jgpps/132006.
- [12] G. Romani, Q. Ye, F. Avallone, D. Ragni, and D. Casalino, "Numerical analysis of fan noise for the NOVA boundary-layer ingestion configuration," *Aerospace Science Technology*, vol. 96, Jan. 2020, doi: 10.1016/j.ast.2019.105532.

- [13] A. Shahsavari and M. Nili-Ahmadabadi, “A novel approach for the design of axial flow fan by increasing by-pass ratio in a constant-diameter turbofan,” *Propulsion and Power Research*, vol. 9, no. 2, pp. 142–158, Jun. 2020, doi: 10.1016/j.jprr.2020.04.005.
- [14] S.-B. Ma, A. Afzal, K.-Y. Kim, J. Choi, and W. Lee, “Optimization of a Two-Stage Transonic Axial Fan to Enhance Aerodynamic Stability,” 2016. [Online].
- [15] J. H. Kim, B. Ovgor, K. H. Cha, J. H. Kim, S. Lee, and K. Y. Kim, “Optimization of the Aerodynamic and Aeroacoustic Performance of an Axial-Flow Fan,” *AIAA Journal*, vol. 52, no. 9, pp. 2032–2044, 2014 doi: 10.2514/1.J052754.
- [16] A. Samad, K. Y. Kim, T. Goel, R. T. Haftka, and W. Shyy, “Multiple Surrogate Modeling for Axial Compressor Blade Shape Optimization,” *Journal of Propulsion and Power*, vol. 24, no. 2, pp. 302–310, 2008, doi: 10.2514/1.28999.
- [17] W. Wang, R. Mo, and Y. Zhang, “Multi-objective Aerodynamic Optimization Design Method of Compressor Rotor based on insight,” in *Proceeding Engineering*, 2011, pp. 3699–3703. doi: 10.1016/j.proeng.2011.08.693.
- [18] A. F. O. Falcão and L. M. C. Gato, “8.05 - Air Turbines,” in *Comprehensive Renewable Energy*, A. Sayigh, Ed., Oxford: Elsevier, 2012, pp. 111–149. doi: <https://doi.org/10.1016/B978-0-08-087872-0.00805-2>.
- [19] J. N. Sørensen, “2.07 - Aerodynamic Analysis of Wind Turbines,” in *Comprehensive Renewable Energy (Second Edition)*, Second Edition., T. M. Letcher, Ed., Oxford: Elsevier, 2022, pp. 172–193. doi: <https://doi.org/10.1016/B978-0-12-819727-1.00127-8>.
- [20] Y. NAKANISHI and K. KAMEMOTO, “Numerical Simulation of Flow around a Sphere with Vortex Blobs,” in *Computational Wind Engineering 1*, S. Murakami, Ed., Oxford: Elsevier, 1993, pp. 363–369. doi: <https://doi.org/10.1016/B978-0-444-81688-7.50040-1>.
- [21] S. Sarkar, A. K. Nag, and R. Kumar, “Chapter 7 - An overview of small-scale hydropower and its recent development,” in *Renewable Energy Production and Distribution*, vol. 2, M. Jeguirim and P. Dutournié, Eds., in *Advances in Renewable Energy Technologies*, vol. 2., Academic Press, 2023, pp. 249–314. doi: <https://doi.org/10.1016/B978-0-443-18439-0.00009-4>.

- [22] C. Baker *et al.*, “Chapter 4 - Computational Techniques,” in *Train Aerodynamics*, C. Baker, T. Johnson, D. Flynn, H. Hemida, A. Quinn, D. Soper, and M. Sterling, Eds., Butterworth-Heinemann, 2019, pp. 53–71. doi: <https://doi.org/10.1016/B978-0-12-813310-1.00004-6>.
- [23] L. Laloui and A. F. Rotta Loria, “Chapter 3 - Heat and Mass transfers in the context of energy geostructures,” in *Analysis and Design of Energy Geostructures*, L. Laloui and A. F. Rotta Loria, Eds., Academic Press, 2020, pp. 69–135. doi: <https://doi.org/10.1016/B978-0-12-816223-1.00003-5>.
- [24] B. Ait-Amir, P. Pougnet, and A. El Hami, “6 - Meta-Model Development,” in *Embedded Mechatronic Systems 2*, A. El Hami and P. Pougnet, Eds., Elsevier, 2015, pp. 151–179. doi: <https://doi.org/10.1016/B978-1-78548-014-0.50006-2>.
- [25] J. Antony, “7 - Fractional Factorial Designs,” in *Design of Experiments for Engineers and Scientists (Second Edition)*, Second Edition., J. Antony, Ed., Oxford: Elsevier, 2014, pp. 87–112. doi: <https://doi.org/10.1016/B978-0-08-099417-8.00007-9>.
- [26] J. S. Rao and B. Kumar, “3D Blade root shape optimization,” in *10th International Conference on Vibrations in Rotating Machinery*, Woodhead Publishing, 2012. doi: <https://doi.org/10.1533/9780857094537.4.173>.
- [27] A. K. Das and S. Dewanjee, “Chapter 3 - Optimization of Extraction Using Mathematical Models and Computation,” in *Computational Phytochemistry*, S. D. Sarker and L. Nahar, Eds., Elsevier, 2018, pp. 75–106. doi: <https://doi.org/10.1016/B978-0-12-812364-5.00003-1>.
- [28] A. J. Strazisar, J. R. Wood, M. D. Hathaway, and K. L. Suder, “NASA Laser Anemometer Measurements in a Transonic Axial-Flow Fan Rotor,” 1989.
- [29] W. Zhang, S. Stapelfeldt, and M. Vahdati, “Influence of the Inlet Distortion on Fan stall Margin at Different Rotational speeds,” *Aerospace Science and Technology*, vol. 98, p. 105668, 2020.
- [30] A. G. Harouni, “Flow Control of a Boundary layer Ingesting Serpentine Diffuser via Blowing and Suction,” *Aerospace Science and Technology*, vol. 39, pp. 472–480, 2014, doi: [10.1016/j.ast.2014.05.016](https://doi.org/10.1016/j.ast.2014.05.016).
- [31] B. Johnson, R. Webster, and K. Sreenivas, “A numerical investigation of S-duct flows with boundary-layer ingestion,” in *48th AIAA Aerospace Sciences Meeting Including the New Horizons Forum and Aerospace Exposition*, 2010, p. 841.

- [32] -i X F, T. F. Gelder, J. F. Schmidt, K. L. Suder, and M.-D. H. -, “Design and Performance of Controlled-Diffusion Stator Compared with Original Double-Circular-Arc Stator (HASA-TB-100141).
- [33] K. L. Suder and M. L. Celestina, “Experimental and Computational Investigation of the Tip Clearance Flow in a Transonic Axial Compressor Rotor,” *Journal of Turbomachinery*, vol. 118, no. 2, pp. 218–229, Apr. 1996, doi: 10.1115/1.2836629.
- [34] E. Benini and R. Biollo, “Aerodynamics of Swept and Leaned Transonic Compressor-rotors,” *Applied Energy*, vol. 84, no. 10, pp. 1012–1027, 2007.
- [35] J. Cong, J. Jing, Z. Dai, J. Cheng, and C. Chen, “Influence of Circumferential Grooves on the Aerodynamic and Aeroelastic Stabilities of a Transonic Fan,” *Aerospace Science and Technology*, vol. 117, p. 106945, 2021.
- [36] D. N. A. G. C. Papageorgakis, “Comparison of Linear and Non-linear RNG-Based k-epsilon Models For Incompressible Turbulent Flows,” *Numerical Heat Transfer, Part B: Fundamentals*, vol. 35, no. 1, pp. 1–22, Feb. 1999, doi: 10.1080/104077999275983.
- [37] J. S. Rao and B. Kumar, “3D Blade root shape optimization,” in *10th International Conference on Vibrations in Rotating Machinery*, Woodhead doi: 10.1533/9780857094537.4.173.
- [38] E. J. Gunn and C. A. Hall, “Aerodynamics of Boundary Layer Ingesting Fans,” 2014.
- [39] P. Okonkwo and H. Smith, “Review of Evolving Trends in Blended Wing Body Aircraft Design,” *Progress in Aerospace Sciences*, vol. 82, pp. 1–23, 2016, doi: <https://doi.org/10.1016/j.paerosci.2015.12.002>.
- [40] N. G. M. Moirou, D. S. Sanders, and P. Laskaridis, “Advancements and Prospects of Boundary Layer Ingestion Propulsion Concepts,” *Progress in Aerospace Sciences*, vol. 138. Elsevier Ltd, Apr. 01, 2023. doi: 10.1016/j.paerosci.2023.100897.

APPENDIX-I

Aerodynamic Performance and Parametric Optimization of Blade Edges under the Influence of Boundary Layer Ingestion

Abstract

A non-axisymmetric inlet distortion problem exists in a boundary layer ingesting propulsion system, which seriously affects the aerodynamic performance of the fan. This work presents an in-depth analysis of the fan stage under the influence of boundary layer ingestion. A high-fidelity numerical approach is adopted to quantify the parameters that reduce the isentropic efficiency, total pressure ratio, and stability margin. At a later stage, an artificial neural network-based surrogate mathematical model is used in a multi-objective genetic algorithm to perform optimization. NASA stage 67 has been selected and validated against the experimental data. Entire annulus, steady-state, and three-dimensional modeling have been used for the combined analysis to analyze the effect of the inlet distortion on the fan stage. The numerical results indicated that the isentropic efficiency and total pressure ratio dropped by 9.49 % and 4.1%, respectively. The significant losses occurred at the suction side of the adjacent blade. Based on losses, trailing edge parameters are selected over the span near the blade's tip to ensure robust performance under the fan-face distortion. As a result of optimization, the isentropic efficiency and total pressure ratio improved by 2.88% and 1.69%, respectively. The optimization adds a value near the tip of the blade caused by the improvement of shockwave.

Journal: Propulsion and Power Research (**Under Review**)